

RESEARCH

Open Access



Anti-inflammatory coupled anti-angiogenic airway stent effectively suppresses tracheal in-stents restenosis

Yanan Zhao^{1,2†}, Yiming Liu^{1,2†}, Jiheng Shan^{1,2}, Xiaohong Xu^{3,4,7}, Chengzhi Zhang^{1,2}, Zaoqu Liu^{1,2}, Xiaomeng Li⁶, Zhaoqian Zhong^{3,4}, Yanxia Gao^{3,4}, Kewei Ren^{1,2}, Dechao Jiao^{1,2}, Jianzhuang Ren^{1,2}, Ping Wu⁵, Yong Jiang^{3,4*} and Xinwei Han^{1,2*}

Abstract

Excessive vascularization during tracheal in-stent restenosis (TISR) is a significant but frequently overlooked issue. We developed an anti-inflammatory coupled anti-angiogenic airway stent (PAGL) incorporating anlotinib hydrochloride and silver nanoparticles using advanced electrospinning technology. PAGL exhibited hydrophobic surface properties, exceptional mechanical strength, and appropriate drug-release kinetics. Moreover, it demonstrated a remarkable eradication effect against methicillin-resistant *Staphylococcus aureus*. It also displayed anti-proliferative and anti-angiogenic properties on human umbilical vein endothelial cells and lung fibroblasts. PAGL was implanted into the tracheae of New Zealand rabbits to evaluate its efficacy in inhibiting bacterial infection, suppressing the inflammatory response, reducing angiogenesis, and attenuating excessive fibroblast activation. RNA sequencing analysis revealed a significant downregulation of genes associated with fibrosis, intimal hyperplasia, and cell migration following PAGL treatment. This study provides insight into the development of airway stents that target angiogenesis and inflammation to address problems associated with TISR effectively and have the potential for clinical translation.

Keywords Anlotinib, Silver nanoparticles, Airway stent, Tracheal in-stents restenosis

[†]Yanan Zhao and Yiming Liu contributed equally to this work.

*Correspondence:

Yong Jiang

jiang48231@163.com

Xinwei Han

fcchanxw@zzu.edu.cn

¹Department of Interventional Radiology, Key Laboratory of Interventional Radiology of Henan Province, The First Affiliated Hospital of Zhengzhou University, Zhengzhou 450001, China

²Interventional Institute of Zhengzhou University, Zhengzhou 450001, China

³State Key Laboratory of Antiviral Drugs, Henan Key Laboratory of Critical Care Medicine, Henan International Joint Laboratory of Infection and Immunology, Department of Emergency Medicine, The First Affiliated Hospital, Zhengzhou University, Zhengzhou 450001, China

⁴Institute of Infection and Immunity, Henan Academy of Innovations in Medical Science, Zhengzhou 450001, China

⁵National Key Laboratory of Macromolecular Drug Development and Manufacturing, School of Pharmaceutical Science, Wenzhou Medical University, Wenzhou 325000, China

⁶School of Mechanics and Safety Engineering, Zhengzhou University, Zhengzhou 450001, China

⁷School of Basic Medicine, Zhengzhou University, Zhengzhou 450051, China



Introduction

Airway stent placement is an effective and timely approach for restoring airway patency and alleviating clinical symptoms in patients with tracheal stenosis [1–3]. Currently, silicone stents and self-expanding metallic stents (SEMS) are the two main types commonly used in clinical practice [3, 4]. However, a high incidence of tracheal in-stent restenosis (TISR) hinders stents' long-term effectiveness and durability [5, 6]. As a continuously expanding foreign body in the tracheal, stents disrupt the tracheal microenvironment, characterized by a sustained inflammatory response, uncontrolled angiogenesis, and highly activated fibroblasts [7–9]. Furthermore, this cascade of events culminates in granulation tissue hyperplasia and TISR deterioration [10–13]. Notably, excessive vascularization plays a critical role in promoting granulation tissue hyperplasia [7, 14, 15]. Therefore, developing an airway stent capable of inducing anti-inflammatory and anti-angiogenic effects to modulate the tracheal microenvironment represents a promising approach for treating TISR.

Recent studies have demonstrated that the severity of the inflammation responses, an upstream initiating factor, could influence the extent of granulation formation [9, 16]. Moreover, airway stent placement can increase microbial colonization, exacerbating the local inflammatory response [17, 18]. Various airway stents coated with anti-inflammatory or antibacterial drugs such as indomethacin [19], dexamethasone [20], doxycycline [21, 22], and vancomycin [23] have been developed to moderate tracheal inflammation response after airway stents placement. Advances in nanotechnology include the potential application of silver nanoparticles (AgNPs) to the biomedical field because of their broad-spectrum bactericidal properties, absence of antibiotic resistance, and enhanced safety profile [24–26]. AgNPs can directly damage the bacterial cell wall or release Ag⁺ to produce reactive oxygen species (ROS) that damage nucleic acids and proteins within the bacteria, ultimately leading to lysis. In addition, AgNPs have shown anti-inflammatory effects by downregulating the expression of interleukin-6 (IL-6), IL-8, and tumor necrosis factor- α (TNF- α) [24, 27]. Consequently, AgNPs show promise as an ideal microbicide and anti-inflammatory agent for mitigating the host response.

In the abnormal tracheal microenvironment, dysregulated growth factors, such as vascular endothelial growth factor (VEGF), fibroblast growth factor (FGF), and transforming growth factor- β (TGF- β), elicit uncontrolled angiogenesis and promote migration of vascular endothelial cells through various signaling pathways [7, 15, 26–34]. Dysregulated neovascularization is critical for the recruitment of inflammatory cells, infiltration and activation of fibroblasts, and transportation of nutrition

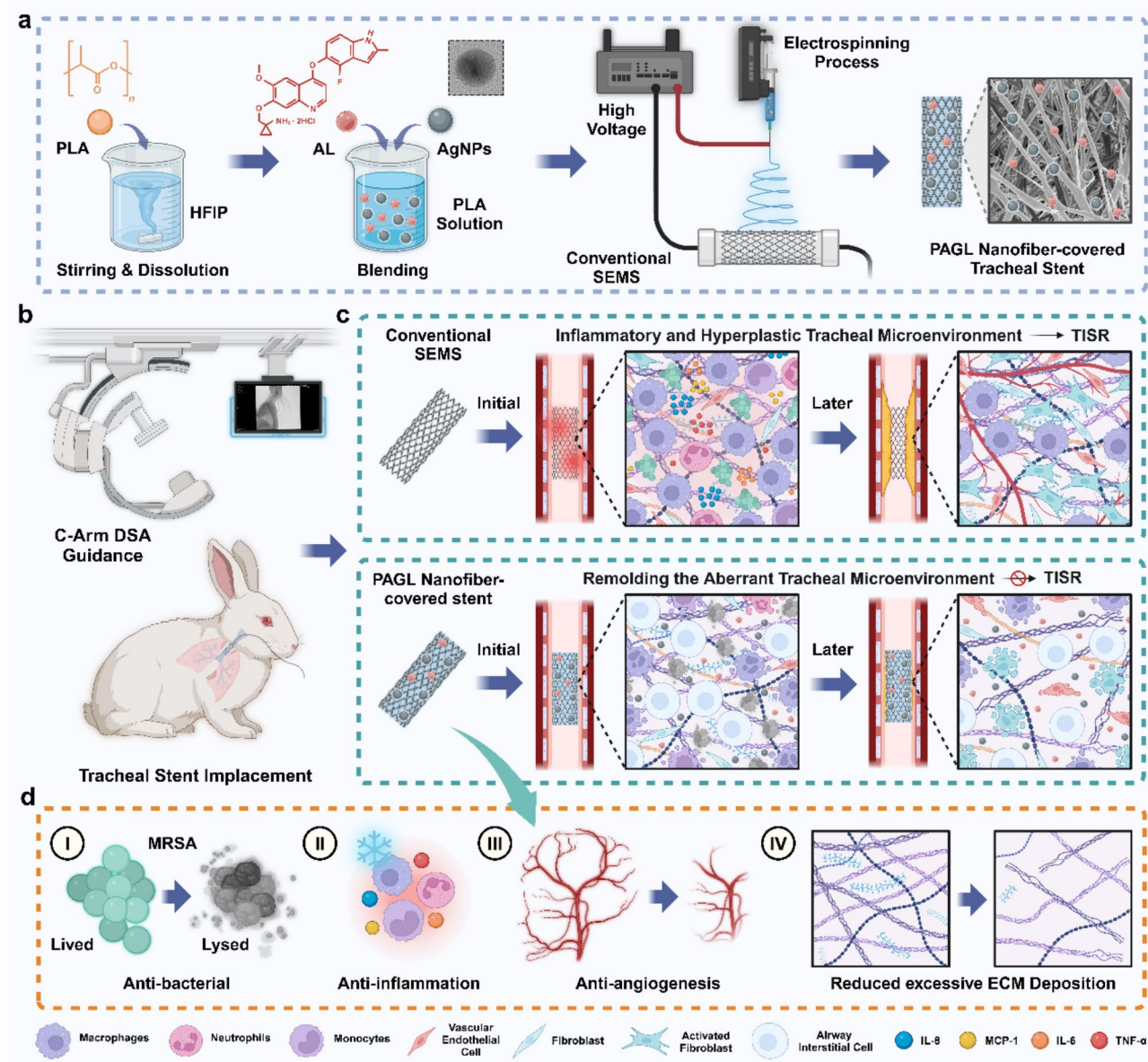
in the tracheal microenvironment [14, 17, 31]. More importantly, activated fibroblasts undergo proliferation and secrete excess collagen, accumulating in the extracellular matrix (ECM) [35, 36]. This situation exacerbates local granulation tissue hyperplasia. Notably, molecular-targeted drugs with synergistic, antagonistic effects on multiple signaling pathways have attracted significant attention [29–31]. Chen et al. fabricated molecular targeted gefitinib-loaded polyurethane foams-covered airway stents to treat bronchotracheal cancer [37]. Unlike traditional nonspecific chemotherapeutic drugs, such as paclitaxel and cisplatin, molecular targeted drugs have a precise mechanism of action and fewer adverse effects. As a novel multi-targeted receptor tyrosine kinase inhibitor, anlotinib hydrochloride (AL) inhibits multiple growth factors receptors for VEGF, FGF, and TGF- β that mediate signaling transduction involved in cell proliferation and angiogenesis [38, 39]. Wu et al. demonstrated that AL can modulate the TGF- β 1 signaling pathway to attenuate bleomycin-induced pulmonary fibrosis [39]. Additionally, Lei et al. reported that AL can modulate VEGFR2-mediated angiogenesis to ameliorate hepatic fibrosis [40]. Therefore, AL should act synergistically with AgNPs to reduce the incidence of TISR events.

With advances in biomedical engineering, electrospun nanofiber films have emerged as a promising drug delivery platform because of their excellent biocompatibility, large specific surface area, and high porosity [41–43]. In this study, a solution of polylactic acid (PLA) co-blended with AgNPs and AL was sprayed onto a framework of a SEMS to fabricate a PLA/AgNPs/AL (PAGL) nanofiber-covered airway stent with anti-angiogenic and anti-inflammatory effects through electrospinning technology (Scheme 1). The physical barrier effect of PAGL nanofiber film not only hinders the granulation tissue hyperplasia across the stent mesh but also reduces the irritating effect of SEMS on tracheal tissue [44]. It serves as a reservoir for the sustained release of AgNPs and AL in situ. Overall, PAGL nanofiber-covered airway stent synergized with AL and AgNPs to ultimately curtail granulation tissue hyperplasia and prevent TISR by inducing bacterial death, downregulating inflammatory mediator levels, suppressing angiogenesis, and inhibiting fibroblasts activation *in vitro* and *in vivo*.

Materials and methods

Materials

Poly(lactic acid) (PLA, $M_w = 110,000$) and 1,1,1,3,3,3-Hexafluoro-2-propanol (HFIP) were provided by Shanghai Macklin Biochemical Technology Co., Ltd. (Shanghai, China). Anlotinib hydrochloride (AL) was supplied by Nanjing Zhengda Tianqing Pharmaceutical Co., Ltd. (Nanjing, China). Silver nanoparticles (AgNPs, purity = 99.99%) were obtained from Shanghai Yurui



Scheme 1 Schematic illustration of the nanofiber-covered airway stent carrying anlotinib hydrochloride (AL) and silver nanoparticles (AgNPs) against tracheal in-stents restenosis (TISR). **(a-b)** The preparation process of the PAGL nanofiber-covered airway stent and its application to the trachea of New Zealand rabbits. **(c)** Unlike the conventional self-expanding metallic stent (SEMS) that results in TISR, the PAGL nanofiber-coated airway stent can remold the inflammatory and hyperplastic tracheal microenvironment to prevent TISR. **(d)** The PAGL nanofiber-coated airway stent effectively prevents TISR by eradicating methicillin-resistant *Staphylococcus aureus* (MRSA), suppressing the inflammatory response, inhibiting the uncontrolled angiogenesis, and subsequent excessive ECM deposition. Created in BioRender. Liu, Y. (2024) <https://BioRender.com/m52f909>

Chemical Co., Ltd. (Shanghai China). Self-expandable metallic stents (SEMS, 20 mm × 8 mm) were purchased from Micro-Tech Medical Technology Co., Ltd (Nanjing, China). Human umbilical vein endothelial cells (HUVECs) and human pulmonary fibroblasts (HPFs) were obtained from the Shanghai Cell Center (Chinese Academy of Sciences). Phosphate-buffered saline (PBS; P4474), Dulbecco’s modified Eagle’s medium (DMEM; D6429), fetal bovine serum (FBS; F8687), penicillin-streptomycin (V900929), and trypsin-EDTA (59417 C) were

supplied by Sigma-Aldrich Trading Co., Ltd. (Shanghai, China). Artificial lysosomal fluid (ALF; BZ257) were obtained from Beijing Eastmo Biotechnology Co., Ltd. (Beijing, China). The Bacterial Viability/Virulence Test Kit (L6060S) was purchased from Shanghai BioScience Co., Ltd. (Shanghai, China). The Live and Dead Cell Double Staining Kit (KTA1001) and Cell Counting Kit-8 (CCK-8; KTA1020) were sourced from Abbkine Scientific Co., Ltd. (Wuhan, China). The Annexin V-FITC/Propidium iodide (PI) Apoptosis Kit (E-CK-A211) was

purchased from Elabscience Biotechnology Co., Ltd. (Wuhan, China). The Cell Cycle and Apoptosis Analysis Kit (C1052) was purchased from Beyotime Biotechnology Co., Ltd. (Shanghai, China). All other chemical and biological reagents were used without modification.

Construction of drug-loaded nanofiber-covered airway stent

A PLA solution was prepared by dissolving 1.25 g of PLA in 10 mL of HFIP. Then, 0.05 g of AgNPs were dissolved in the PLA solution to create a PLA/AgNP solution. Similarly, 0.01 g of AL was dissolved in the PLA solution to create a PLA/AL solution. Finally, the PLA/AgNPs/AL solution was prepared by combining the two solutions above with the PLA solution (Table S1). Drug-loaded nanofiber-covered airway stents (PLA, PAG, PAL, and PAGL) were prepared using SEMS in the expanded state as a backbone to receive an electrospun nanofiber overlay using an electrospun system. The solutions underwent electrospinning with a high-voltage power supply set at 15 kV, a flow rate of 0.5 mL/h, and a drum collector positioned 20 cm away from the needle tip. The SEMS in the expanded state were nested and aligned on a drum collector, and the nanofibers were ejected from the tip and collected as the drum rotated. To ensure a relatively consistent thickness of nanofiber films on the surface of the four groups of stents, 1.7 mL of the electrospun solution was applied to each SEMS based on multiple preliminary experiments. The final nanofiber-covered airway stents were constructed at a length of 2 cm and a diameter of 0.8 cm and named PLA, PLA/AgNPs (PAG), PLA/AL (PAL), and PLA/AgNPs/AL (PAGL) based on their drug loads, respectively. The stents were dried and stored in sealed containers at 4 °C for future use.

Surface physicochemical characterization

Transmission electron microscopy (TEM, JEM-2100 F; JEOL, Japan) was used to identify the particle size and morphology of the AgNPs. Fourier transform infrared spectroscopy (FTIR, TNZ1-5700; Nicolet, USA) of the samples was performed with a scanning range of 500–4000 cm^{-1} . Raman spectroscopy (DXR2; Thermo Fisher Scientific) further examined the chemical groups. The surface morphology and elements were observed using scanning electron microscopy (SEM, JSM-7401 F; JEOL, Japan) with an energy dispersive spectrum (EDS) analysis system. Using the Laplace-Young method, the water contact angle was measured with a contact angle measuring device (Portsmouth, USA). The mechanical properties were tested by a universal testing machine (CMT6503; Shenzhen SANS Test Machine, China) at a tensile rate of 10 mm/min. The tensile strength of the samples was recorded.

In vitro drug-release behavior

The nanofiber films were cut into approximately 10 mg small cubes, which were submerged in 5 mL of PBS and agitated at 50 rpm and 37 °C to evaluate the samples' drug-release behavior. At specific times (0–21 days), 1 mL of the sustained-release solution was collected for testing and subsequently replaced with 1 mL of fresh PBS. A UV-VIS spectrophotometer (model 3700, Shimadzu, Japan) was used to measure the absorbance at 411 nm and 222 nm to determine the amount of released AgNPs and AL in the release medium (i.e., PBS at pH 7.4), respectively. The percentage of released AgNPs and AL was calculated based on the initial weight of the AgNPs and AL in the electrospun nanofiber films.

Antibacterial performance evaluation

Methicillin-resistant *Staphylococcus aureus* (MRSA, ATCC 33592) was used to test the effectiveness of the nanofiber films against drug-resistant bacteria. Six groups were established: B.C., P.C., PAG, PAL, and PAGL. The nanofiber films were cut into $1 \times 1 \text{ cm}^2$ squares and exposed for 30 min under ultraviolet (UV) light for sterilization and subsequent assays. The bacterial proliferation, clone formation, and live/dead bacterial staining assays were used to assess the viability and proliferation capacity of the treated bacteria. Please refer to the [supporting information](#) for the detailed protocols.

In vitro anti-angiogenesis and anti-hyperplasia

The HUVECs and HPFs were evaluated to determine the effects of anti-angiogenesis and anti-hyperplasia, respectively. The experiments were divided into the following four groups: a blank control group (BC), a PAG nanofiber film group (PAG), a PAL nanofiber film group (PAL), and a PAGL nanofiber film group (PAGL). The nanofiber films were cut into $1 \times 1 \text{ cm}^2$ squares and exposed to UV light for 30 min for sterilization and subsequent assays.

Live/Dead cell staining and CCK-8 assay

The effect of nanofiber films on cell activity and cell proliferation of HUVECs or HPFs was assessed by Live/dead cell staining and CCK-8 assay, respectively. See the [supporting information](#) for detailed protocols.

Cell apoptosis assay

HUVECs ($3 \times 10^5/\text{mL}$) were co-incubated with the samples at 37 °C, washed with PBS, and trypsin-digested into single-cell suspensions. The cells were then stained with Annexin V-FITC and PI for 20 min in the dark and analyzed by flow cytometry (NOVOCyte3130, ACEA, America).

Cell cycle assay

HPFs were co-incubated with the samples at 37 °C, digested with EDTA-free trypsin, centrifuged at approximately 1000 ×g for 3–5 min, and washed with ice-cold PBS. Subsequently, 1 ml of ice-cold 70% ethanol was added, and the cells were fixed at 4°C for 30 min. Following centrifugation, the cells were washed with ice-cold PBS and resuspended. PI staining solution was prepared based on the manufacturer's instructions, and 0.5 ml of PI staining solution was added to each cell sample. The cell precipitates were resuspended slowly in a 37°C bath that was protected from light for 30 min. The red fluorescence at an excitation wavelength of 488 nm was detected using flow cytometry and light scattering.

Scratch assay

HUVECs or HPFs (1×10^5 /mL) were seeded into 6-well plates. After forming a monolayer, a scratch was introduced with a sterile P200 pipette tip, and the floating cells were removed by rinsing with PBS. Subsequently, the corresponding treatments were added to each well to represent the various groups. Photographs of HUVECs or HPFs were taken under a fluorescence microscope (IX53, Olympus, Japan) at 0 and 24 h, respectively. The wound closure rates were calculated using the following formula: Wound closure rate = $(W_0 - W_{24}) / W_0 \times 100\%$. W_0 , wound area at 0 h; W_{24} , wound area at 24 h.

Transwell assay

HUVECs (5×10^4 /mL) were seeded into the upper compartment of a Transwell chamber. Subsequently, the corresponding treatments were added to the upper chamber for the different groups. After incubation for 36 h, the migrating cells retained on the upper surface of the filter film were removed with a cotton swab. The migrating cells on the lower surface of the filter were stained with 0.5% crystal violet solution, fixed in 4% paraformaldehyde, and examined by light microscopy. The number of migrating cells in each group was analyzed using ImageJ software (National Institutes of Health, Bethesda, USA).

Immunofluorescence staining of VEGFR2

HUVECs (1×10^5 /mL) were seeded onto coverslips, treated for 1 d, and fixed with 4% paraformaldehyde solution for 15 min, followed by 0.1% Triton X-100. The cells were then blocked with goat serum at 25°C for 0.5 h. The HUVECs were incubated with an anti-VEGFR2 primary antibody, and samples were incubated with a Cy3-labeled secondary antibody (Table S2 and S3). The cell nuclei were stained with 4',6-diamidino-2-phenylindole (DAPI). A fluorescence microscope was used for data acquisition, and ImageJ was used for data analysis.

Quantitative RT-PCR for VEGFR2 analysis

HUVECs were seeded into 12-well plates and incubated with nanofiber films for 24 h. Subsequently, the cells were collected and washed twice with precooled PBS. Total RNA was extracted by adding 1 mL of TRIzol and reverse-transcribed into cDNA using the cDNA generation kit. Then, 1 μL of cDNA, oligonucleotide primers, 12.5 μL of SYBR® Premix Ex Taq™ II, and DEPC water were added to 25 μL of the reaction. Gene-specific primer pairs were added based on the target gene. Real-time PCR was performed using an ABI-7500 Sequence Detection System (Thermo Fisher Scientific, USA). The Ct values were analyzed by the 2- $\Delta\Delta$ CT method, and glyceraldehyde-3-phosphate dehydrogenase (GAPDH) mRNA was used as an internal control to determine the target gene's relative expression (VEGFR2). Table S4 lists the primers.

Anti-inflammatory coupled anti-angiogenic airway stent prevents TISR in vivo

All implantation procedures were approved by the animal care committee of the First Affiliated Hospital of Zhengzhou University and were conducted based on the guidelines set forth by the National Institute of Health for the care and use of laboratory animals. Twenty male New Zealand rabbits were obtained from the laboratory animal center of Hualan Biological Co., Ltd. (Henan, China). The rabbits were randomly assigned to four groups: the commercial airway stent group (Ctrl), the PAG-covered airway stent group (PAG), the PAL-covered airway stent group (PAL), and the PAGL-covered airway stent group (PAGL).

In vivo airway stent implantation

The New Zealand rabbits were administered anesthesia through intramuscular injection before the procedure. Under fluoroscopic guidance using the Artis zee DSA system (Siemens, Germany), the animals were supine with their necks hyperextended. The entire process was carried out using a 5-Fr stent delivery system. An entrance dilation was performed using a 12-Fr dilator (12-F dilator, Cook Medical). Subsequently, an intratracheal channel was created using a 0.035-inch guidewire (Terumo Corporation; Tokyo, Japan) and a 5-Fr catheter (Terumo Corporation; Tokyo, Japan). The delivery system along with the stent was advanced over the guidewire, and the stent was positioned at least 1.5–2 cm cranially to the carina. Following stent placement, the animals were closely monitored and euthanized four weeks later.

Computed tomography

Four weeks after stenting, computed tomography scans (CT, Sensation 64, Siemens, Germany) of the neck and chest were performed on the rabbits to visualize the

airway condition, stent morphology, and granulation tissue hyperplasia. Slices (1 mm-thick) with 0.5 mm intervals were used, and multiplanar reconstruction was performed. Before CT examination, anesthesia was administered by xylazine hydrochloride injection at 0.02 ml/kg intramuscularly. After the anesthesia took effect, the animals were fixed on the CT table to complete the scanning. Data and images were analyzed using Siemens image postprocessing software.

In vivo antibacterial assessment

Four weeks after stent placement, the rabbits were euthanized using pure carbon dioxide inhalation. Nanofiber films were carefully peeled from the various stents to assess the *in vivo* antimicrobial effect. The films were washed three times with a sterile saline solution and sonicated with 1 mL of sterile saline solution for 30 s to collect the bacteria. The resulting bacterial suspension was appropriately diluted and inoculated onto solid culture substrates to compare the intratracheal bacterial content among the different groups. The relationship between the intratracheal bacterial content and the growth of the granulation tissue was analyzed using linear regression.

Histopathological evaluation

After stent removal, the trachea was incised transversely, near the proximal and distal ends of the airway stent, to obtain tracheal specimens. These specimens were paraffin-embedded, sectioned, and subjected to various staining. Following established methods, Hematoxylin and eosin (H&E) and Masson's trichrome (MT) staining were used to evaluate inflammation and the degree of granulation tissue hyperplasia. The other tissue sections from the tracheal specimens were stained with antibodies against Caspase-3, Ki67, CD31, α -smooth muscle actin (α -SMA), and a polarized light Sirius scarlet stain. The corresponding data for the antibodies used is listed in Table S2. In addition, the serum liver and renal function tests were done to evaluate the biosafety of airway stents.

Enzyme-linked immunosorbent assay (ELISA)

The various tracheal tissue groups were thoroughly washed and finely pulverized to prepare homogenates. The supernatant was centrifuged at 5000 \times g for 5 min. Working solutions for each component were prepared following the manufacturer's instructions. The 50 μ L of the samples and 100 μ L of horseradish peroxidase-labeled detection antibody were added for each well. The reaction plate was covered with a sealing pad and incubated at 37°C for 60 min in the dark. The wells were then washed five times with a washing solution. Next, 100 μ L of the substrate mixture was added to the wells, and the plate was incubated at 37°C for 15 min. Finally, 50 μ L of termination solution was added to the wells. The optical

density (OD) of each well was measured using a microplate analyzer (NanoDrop, Thermo Fisher, USA) to measure the levels of IL-8, monocyte chemoattractant protein-1 (MCP-1), IL-6, and TNF- α (Table S6).

Tracheal tissue qRT-PCR of VEGFR2, α -SMA, and Col IIIa1

The tracheal tissues were thoroughly washed and finely ground to prepare homogenates. Total RNA from granulation tissue was extracted using TRIzol and reverse transcribed into cDNA using M-MLV reverse transcriptase. The real-time PCR was performed on a real-time PCR system using SYBR reagent, and Table S5 lists the primer sequences for the three targets.

Transcriptome sequencing and high-throughput analysis

The tracheal tissue from the Ctrl and PAGL groups was flash-frozen in liquid nitrogen and subsequently pulverized into a fine powder. Total RNA was extracted from the tissue using TRIzol reagent, and the RNA was quantified using a UV spectrophotometer. Digital gene expression tag profiling was conducted by GENOSEQ Co. Ltd. (Wuhan, China). GO enrichment analyses, Gene Set Enrichment Analysis, and protein-protein interaction (PPI) analysis were done following standard protocols.

Statistical analyses

All results are presented as the mean \pm SD. Two-group comparisons were performed using a Student's *t*-test, whereas a one-way ANOVA was used for multiple comparisons. GraphPad Prism 8.0 software was used for all statistical analyses. Statistical significances were indicated as follows: not significant, * P < 0.05, ** P < 0.01, and *** P < 0.001.

Results

Physicochemical properties

AgNPs and AL were loaded into PLA to prepare surface nanofibers covered on the SEMS using an electrospinning technique to endow the airway stent with the dual functions of antibacterial and anti-hyperplasia properties. Morphology and particle size were evaluated because the smaller diameter of the AgNPs has stronger antibacterial activity. TEM revealed that the AgNPs exhibited a spherical-like shape with a diameter range of 10–15 nm, which provided a foundation for favorable antibacterial performance at subsequent stages (Fig. 1a). Fourier transform infrared spectroscopy (FTIR)-derived spectra for AgNPs, AL powder, PLA, PAG, PAL, and PAGL were acquired to determine their respective chemical compositions. The FTIR spectra of the AgNPs (Fig. S1a) exhibited three characteristic peaks representing the stretching vibration, including the ether bond at 1072 cm^{-1} , the aromatic ring of the C=C group at 1617 cm^{-1} , and the methylene group at 1384 cm^{-1} , which reflects the residues of the

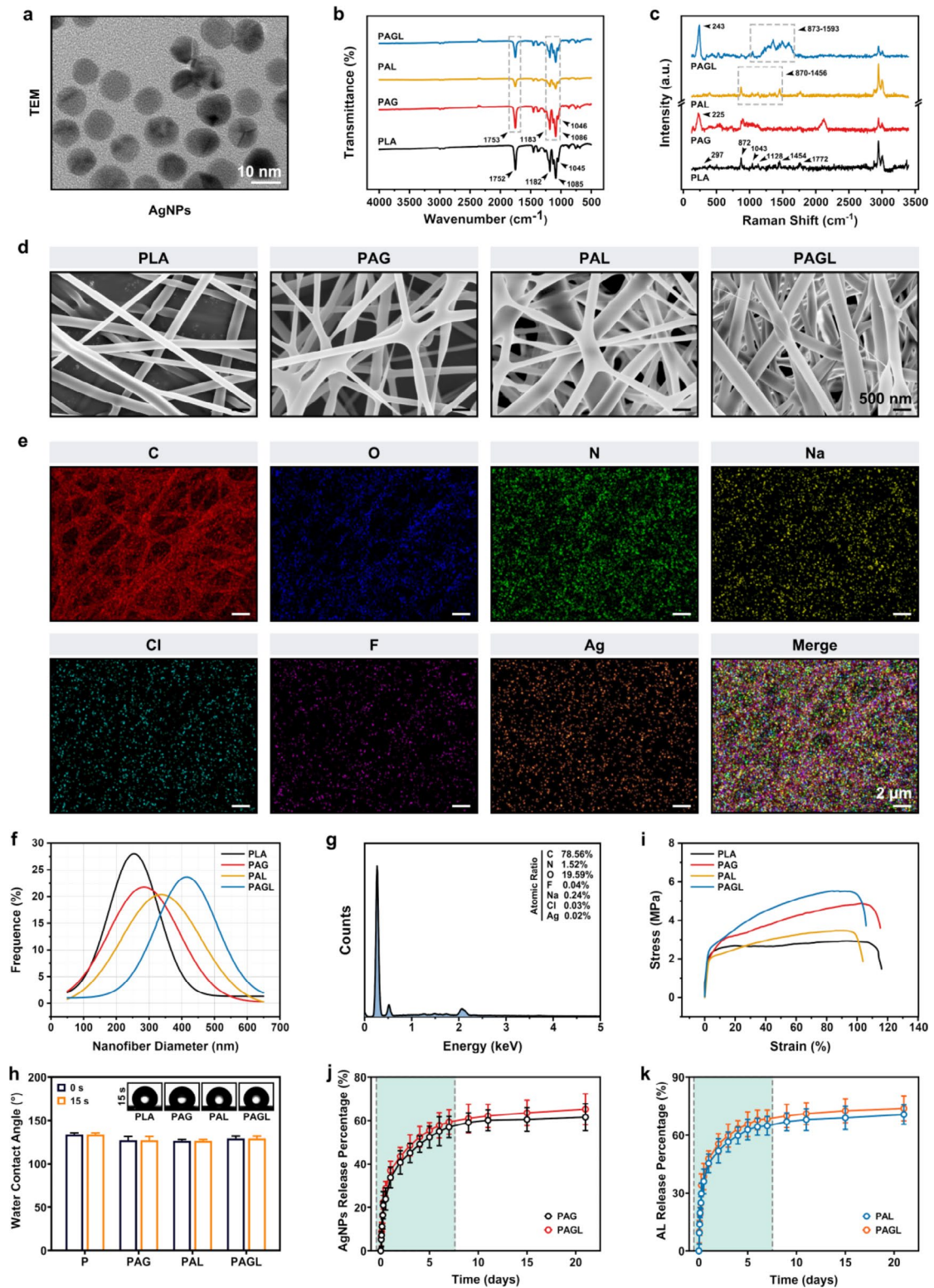


Fig. 1 Physicochemical properties, mechanical properties, and drug-release behavior of nanofiber films covered on the stent surfaces. **(a)** TEM image of AgNPs. **(b)** FTIR spectra and **(c)** Raman spectra of PLA, PAG, PAL, and PAGL nanofiber films, respectively. **(d)** SEM images of PLA, PAG, PAL, and PAGL nanofiber films, respectively. **(e)** EDS elemental mapping results of PAGL nanofiber films. **(f)** The fitted curve of fiber diameter distribution for PLA, PAG, PAL, and PAGL, respectively. **(g)** EDS spectra of PAGL nanofiber films. **(h)** Water contact angle images and statistical analyses. **(i)** Typical stress-strain curves of all nanofiber films. **(j)** AgNPs release profile from PAG and PAGL for 0–21 days at 37 °C, respectively. **(k)** AL release profile from PAG and PAGL for 0–21 days at 37 °C, respectively. Scale bar: 10 nm, 500 nm, and 2 μm

raw materials on the surfaces of the AgNPs before synthesis [45]. The characteristic peaks of AL were at 1021 and 1081 cm^{-1} and attributed to the two C-O ether bond vibrations, at 1425–1618 cm^{-1} to the aromatic ring backbone vibration, at 2911 and 2947 cm^{-1} to the methyl group stretching vibration, at 3293 cm^{-1} to the cyclopropyl group stretching vibration, and at 3403 cm^{-1} to the secondary amine group vibration [46]. As shown in Fig. 1b, the typical peaks of the PLA nanofibers appeared at 1752 cm^{-1} with C=O stretching, 1453 cm^{-1} associated with CH bending, 1182 cm^{-1} with C-O-C stretching, 1129 and 1085 cm^{-1} with C-O stretching and 1045 cm^{-1} attributed to OH bending [47]. Although the PAG, PAL, and PAGL nanofiber films exhibited typical characteristic peaks of PLA with slight shifts, the characteristic peaks of the AgNPs and AL were masked and insignificant.

Raman spectroscopy was used to analyze the chemical groups of the raw materials and electrospun nanofiber films. As shown in Fig. S1b, the AgNPs yielded a characteristic peak at 238 cm^{-1} , representing the Ag-O bond of the oxidized AgNPs. AL exhibited two characteristic peak populations at 886–1468 cm^{-1} and 2918–2976 cm^{-1} . The former was attributed to carbon-fluorine bonding, ether bonding, and aromatic backbone vibrations, whereas the latter was attributed to the C-H bond stretching vibration [48]. Figure 1c shows that the characteristic peaks of the PLA nanofiber films appearing at 297 cm^{-1} were assigned to C-O-C bending, at 399 cm^{-1} attributed to C-COO stretching, at 872 cm^{-1} to C-CO group vibration, at 1043 cm^{-1} to C-CH₃ skeletal stretching, 1128 cm^{-1} to CH₃ asymmetric rocking, 1454 cm^{-1} to CH₃ symmetric bending, 1772 cm^{-1} to C=O asymmetric stretching, and 2945 cm^{-1} to CH₃ symmetric stretching [49, 50]. The major characteristic peaks of the raw components were shifted and observed at 243 cm^{-1} and 873–1593 cm^{-1} in PAGL nanofiber films, except for the aforementioned characteristic peaks of the PLA. These spectra confirmed that AgNPs and/or AL were successfully introduced into the nanofibers.

The apparent morphology and fiber diameter of the nanofiber films were evaluated by SEM. The nanofiber films exhibited a distinctive randomly interconnected fibrous network structure (Fig. 1d). As shown in Fig. 1f, the average diameters of the PLA, PAG, PAL, and PAGL fibers gradually increased. Moreover, Fig. 1e shows the element mapping of a portion of the PAGL, in which carbon, nitrogen, oxygen, fluorine, sodium, chlorine, and silver were uniformly distributed throughout the nanofibers (Fig. 1g). This further confirms that the AL and AgNPs were successfully loaded onto the nanofibers.

Water contact angle experiments evaluated the hydrophobicity of all the nanofiber films. As shown in Fig. 1h, the droplet morphology on all samples remained essentially unchanged after stabilization (15 s) compared with

the fresh contact, and the water contact angles were $133.7^\circ \pm 2.1^\circ$, $127.3^\circ \pm 4.2^\circ$, $126.7^\circ \pm 1.5^\circ$, and $129.3^\circ \pm 2.5^\circ$ with no statistically significant difference compared with the initial sample. The results suggest that the content of AgNPs and AL doped in this study did not affect the overall hydrophobicity of the films, which may be beneficial in preventing sputum adhesion and improving airway cleanliness [45].

The in vitro degradation behavior of PLA, PAG, PAL, and PAGL samples in PBS and ALF was tested (Fig. S2). In PBS, the residual mass percentage of PAG, PAL, and PAGL was lower than that of the PLA group, which may result from interrupting the fiber's original structure by adding AgNPs and AL. In ALF (pH = 7.0 or 6.5), the residual mass percentage in all groups was lower than in PBS, which was attributed to the weakly acidic environment and the hydrolase component of ALF, which improved degradation. At day 28, the residual mass percentage of PAGL in ALF at pH = 7.0 and 6.5 was only $80.69\% \pm 3.78\%$ and $75.76\% \pm 3.14\%$, respectively. This result indicates that PAGL was gradually degraded with the extension of time, meeting the needs of graft transplantation.

Mechanical properties and drug-release behavior

The favorable mechanical properties of nanofiber films are necessary for the in vivo application of airway stents with surface coating [51–53]. The analysis of stress-strain curves in tensile tests (Fig. 1i) revealed that the introduction of AL slightly reduced the nanofiber film's ductility compared with PLA alone; however, incorporating AgNPs and/or AL enhanced the mechanical strength of the nanofiber film significantly, with PAGL demonstrating the highest mechanical strength. As shown in Fig. S3, the tensile strength of PAGL was 5.17 ± 0.43 MPa, which was higher than that of the remaining three nanofiber films. Thus, the fabricated nanofiber films show suitable mechanical properties for in vivo use.

Subsequently, the in vitro drug-release behavior of PAG, PAL, and PAGL nanofiber films was explored in PBS (PH = 7.4, 37 °C). Overall, the release of AgNPs and/or ALs from all nanofibers can be divided into two burst release phases (0–7 d) and constant release phase (8–21 d). The first burst release rapidly exerts drug efficacy to achieve anti-inflammatory and anti-proliferative effects in a relatively short period. In contrast, the later slow and steady release maintains a certain drug concentration locally to exert drug effects continuously. Specifically, PAG and PAGL in PBS exhibited explosive drug release of AgNPs during the first 7 days, with release percentages of $57.03\% \pm 4.89\%$ and $59.38\% \pm 5.64\%$, respectively (Fig. S4a). After that, AgNPs within the nanofiber films were released slowly and uniformly within the PBS solution for 21 days, with release percentages of $61.7\% \pm 6.16\%$ and $65.23\% \pm 7.12\%$, respectively, with no significant

difference (Fig. 1j). Similar to the former, the PAL and PAGL nanofiber films showed release percentages of $64.83\% \pm 4.84\%$ and $68.38\% \pm 4.65\%$ during the first 7 days, respectively, followed by a slow release during the subsequent 8–21 d (Fig. S4b and 1k).

In vitro antibacterial performance

Infections with drug-resistant pathogens, such as MRSA, remain a thorny issue for airway stents placement, which may lead to severe pneumonia or even patient death [54, 55]. Thus, it is clear that constructing antibacterial airway stents is essential to reduce the risk of MRSA infection. In this work, nanofiber films loaded with AgNPs were used to confer antibacterial properties to airway stents but were next evaluated for their effectiveness at inhibiting MRSA. As shown in Fig. 2b, after co-incubation of the PAG and PAGL nanofiber films containing AgNPs with MRSA, the OD values at 600 nm were significantly lower than those of the BC and PAL groups, indicating that AgNPs can significantly inhibit MRSA proliferation. Moreover, bacterial colony formation was significantly reduced in the presence of AgNPs (Fig. 2c), and the MRSA inhibition rates in the PAG and PAGL groups reached $80.56\% \pm 6.50\%$ and $83.81\% \pm 8.32\%$, respectively (Fig. S5). In a live/dead bacterial staining assay of the treated MRSA, similar intense red fluorescent signals resulting from dead cells appeared in the PAG and PAGL groups, but the PAL group showed only sporadic bacterial death (Fig. 2d). Further statistical analysis showed that the MRSA viability in the PAG and PAGL groups were only $26.30\% \pm 5.08\%$ and $22.00\% \pm 6.12\%$, respectively, which was lower compared with that in the BC and PAL groups (Fig. S6).

To further explore the mechanism of MRSA inhibition by AgNPs in nanofiber films, the production of ROS within MRSA was examined by flow cytometry (Fig. 2e). The relative mean fluorescence intensity (MFI) of ROS within MRSA in the PAG and PAGL groups was obviously increased compared with that in the BC and PAL groups, respectively (Fig. 2f). In addition, protein leakage from MRSA treated with BC and PAL nanofiber films was only about 0.23 ± 0.05 and 0.28 ± 0.12 mg/mL, respectively, whereas the MRSA protein leakage of MRSA treated with PAG and PAGL were significantly increased to 0.82 ± 0.07 and 0.89 ± 0.11 mg/mL, respectively (Fig. 2g). These results may be attributed to the fact that AgNPs or Ag^+ released from PAG and PAGL nanofiber films can trigger bacterial oxidative stress that damages bacterial proteins and DNA, and disrupts the cell wall of MRSA, leading to leakage of bacterial contents and ultimately MRSA death (Fig. 2a).

In vitro anti-angiogenesis performance

Similar to the abnormal damage repair process triggered by other foreign bodies, the TISR process after airway stent placement is accompanied by growth factor disorders (e.g., VEGF and bFGF) and uncontrolled angiogenesis [7, 17, 56]. This massive neovascularizations triggers a cascade of events that increase the infiltration of inflammatory cells and fibroblasts, the diffusion of inflammatory cytokines, and collagen deposition [56–58]. Programming aberrant angiogenesis may be necessary to prevent TISR. Because of the AgNPs and AL properties, the nanofiber film-mediated anti-angiogenic effect was investigated at the cellular level. The results of the live/dead cell staining assay (Fig. 3b, S7) demonstrated that incubation of HUVECs with PAG, PAL, and PAGL for 48 h led to a gradual decrease in the proportion of live cells exhibiting green fluorescence, with PAGL reaching $79.31\% \pm 3.58\%$. These findings suggest that AgNPs and AL induced partial cell death in HUVECs while inhibiting excessive blood vessel growth within granulation tissue regions, thereby impeding oxygen and nutrient supply and reducing in-stents restenosis incidence. As depicted in Fig. 3c, compared to the BC group, OD values for PAG, PAL, and PAGL all exhibited a decreasing trend over time; notably, PAGL displayed the most significant decline. This suggests that PAGL effectively reduces HUVECs activity and proliferation. On one hand, AgNPs induce excessive production of reactive oxygen species (ROS), leading to suborgan damage such as mitochondria and lysosomes dysfunction followed by cell death [59, 60]. On the other hand, AL acts as a multi-target anti-angiogenic drug by interfering with endothelial cell proliferation through inhibition of downstream signaling pathways mediated by angiogenesis-related VEGFRs [39, 61]. Together they synergistically contribute to PAGL displaying the lowest OD value on day 3. However, over time excess drugs are eliminated from the body through metabolism without causing evident toxic side effects on overall health. Furthermore, numerous studies have confirmed that appropriate concentrations of AgNPs and AL have been widely utilized in treating various diseases [62, 63]. Moreover, a classical cell apoptosis assay (cells co-stained with Annexin V-FITC and PI) was performed (Fig. 3d). The results indicated that the PAGL significantly promoted the apoptosis of cells compared with the other groups (Fig. 3f).

The migration ability of the HUVECs was evaluated by a scratch assay and a Transwell assay (Fig. 3e). As seen in Fig. 3g, the closure rate of the cell-free gap in the BC group was approximately $80.13\% \pm 7.58\%$, whereas the PAGL-treated HUVECs showed the largest cell gap ($8.93\% \pm 2.22\%$) after 24 h. In the Transwell assay, HUVECs in the BC group readily passed through the membrane and covered nearly the entire lower surface.

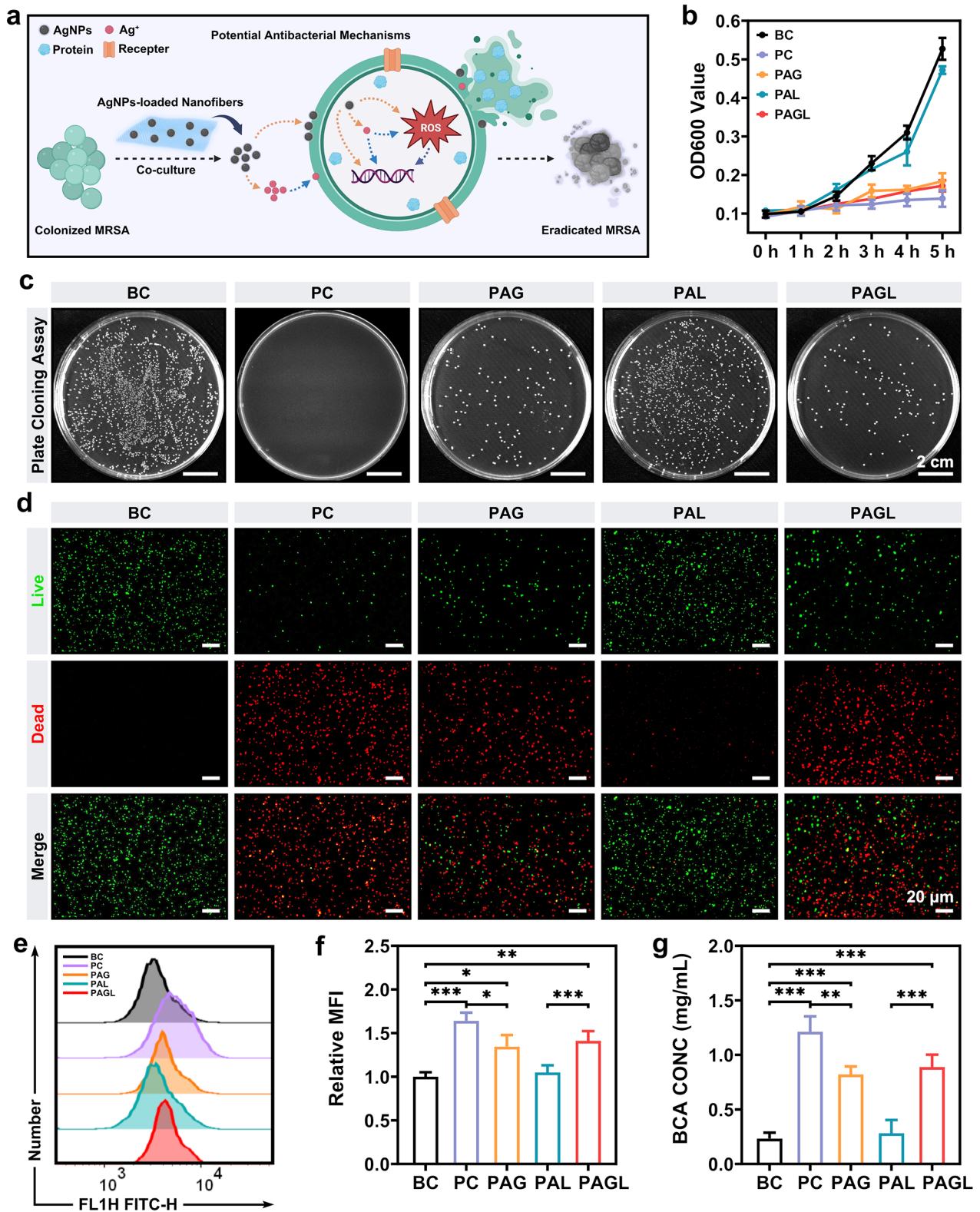


Fig. 2 Antibacterial performance of the nanofiber films covered on the stent surface. **(a)** Mechanism diagram for the inhibition of bacterial growth by the nanofiber films. **(b)** The proliferation of MRSA. **(c)** Representative colony formation images of MRSA. **(d)** Representative live/dead bacterial assay of MRSA. **(e-f)** The fluorescence intensity histograms and relative mean fluorescence intensity (MFI) of the intracellular ROS levels in MRSA. **(g)** Protein leakage analysis of MRSA. Scale bar: 20 μm and 2 cm. Significantly different: **P* < 0.05, ***P* < 0.01, and ****P* < 0.001

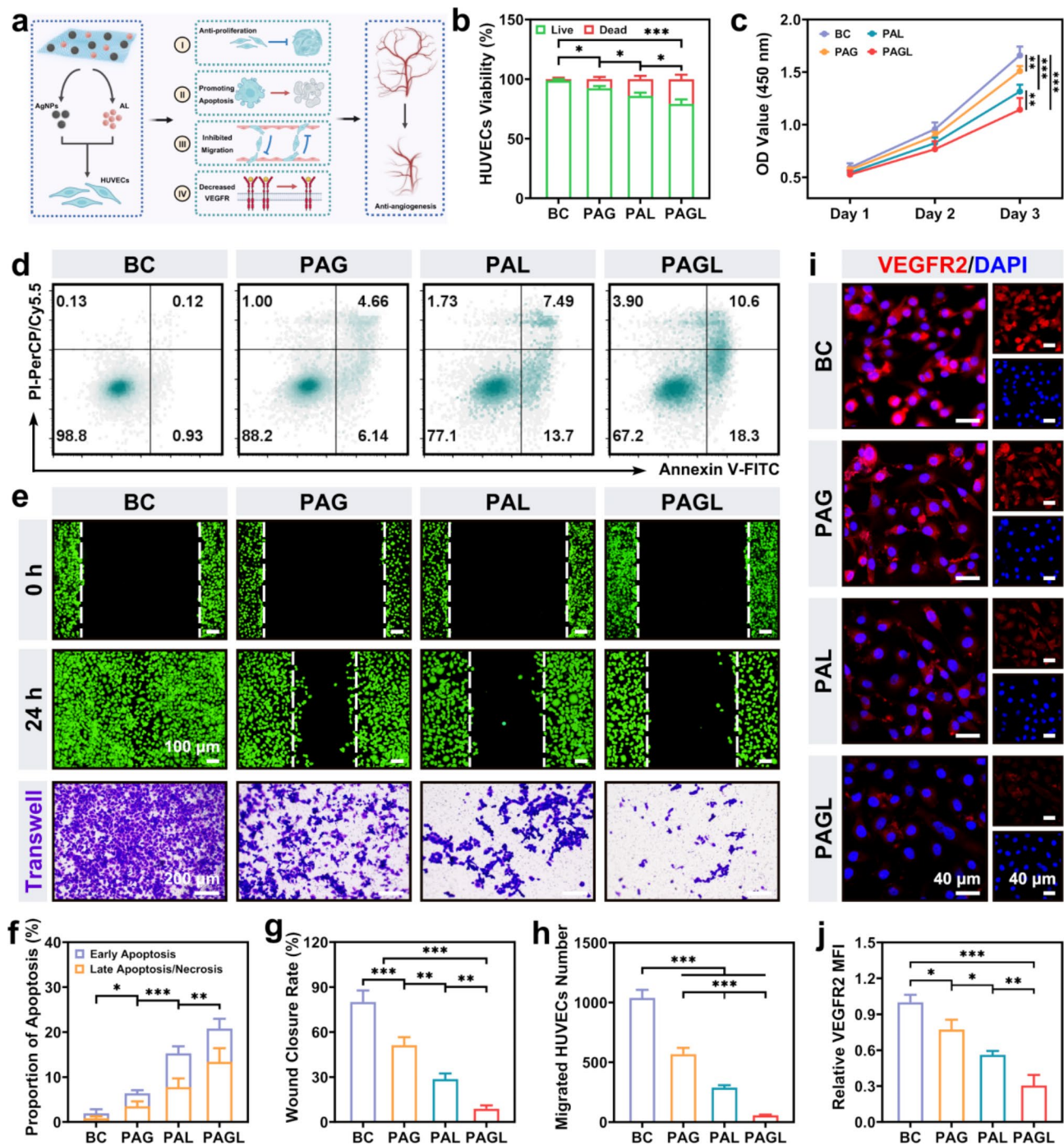


Fig. 3 In vitro anti-angiogenic effect of the nanofiber films covered on the stent surface. (a) Schematic illustration of anti-angiogenic mediated by PAGL. (b) Statistical analysis of HUVECs viability. (c) Cell proliferation of HUVECs over three consecutive days by CCK-8 assay. (d) Flow cytometry to detect cell apoptosis in HUVECs stained with Annexin V/PI. (e) Scratch assay and Transwell assay of HUVECs. (f) The proportion of apoptosis based on the cell apoptosis assay for HUVECs. (g) Quantitative results of the wound closure rate. (h) Quantitative results of the migrating HUVECs number. (i) Representative VEGFR2 immunofluorescence staining of HUVECs. (j) Statistical analysis of the relative mean fluorescence intensity (MFI) for VEGFR2 in HUVECs. Scale bar: 40, 100, and 200 μ m. Significant differences: * $P < 0.05$, ** $P < 0.01$, and *** $P < 0.001$

The number of migrating cells in the BC group was 1038.00 ± 67.51 , indicating that HUVECs exhibit strong migration ability; however, the number of migrating cells in PAG, PAL, and PAGL was decreased to 568.33 ± 51.93 ,

288.00 ± 20.07 , and 56.67 ± 5.69 , respectively (Fig. 3h). The results indicate that the synergistic effect of AgNPs and AL may effectively inhibit the migration capacity of HUVECs.

The highly activated VEGFA-VEGFR2 signaling axis plays a critical role in uncontrolled angiogenesis [64–66]. Specifically, VEGFA induces vascular endothelial cell proliferation, migration, and angiogenesis by binding to VEGFR2 in vascular endothelial cells [66–68]. In Fig. 3i, immunofluorescence staining analysis of intracellular VEGFR2 in treated HUVECs showed that the relative MFI of VEGFR2 in the PAG, PAL, and PAGL groups gradually decreased compared with that in the BC group, with the PAGL group being the most significant (Fig. 3j). This effect may be attributed to the ability of both AgNPs and AL to inhibit the survival of HUVECs by intervention in VEGFA-VEGFR2-mediated angiogenesis [38, 69–72]. Therefore, the novel compound PAGL can synergistically interact with AgNPs and AL, effectively suppressing the proliferation, promoting apoptosis, inhibiting the migration of HUVECs, and ultimately achieving anti-angiogenic effects by downregulating the expression of VEGFR2 (Fig. 3a).

In vitro anti-hyperplasia performance

Fibroblasts are the major cellular component of granulation tissue in the TISR and the primary carrier cells that regulate ECM synthesis and remodeling [7, 13, 73]. For this purpose, HPFs were used to evaluate the anti-hyperplasia effect of nanofiber films in vitro. As depicted in Fig. 4a, the cell morphology of HPFs gradually transformed from normal multi-antennae long shuttle shape to non-antennae cell morphology after PAG, PAL and PAGL treatment compared to the BC group. Additionally, an increasing trend was observed in the number of red fluorescent dead cells. The proportion of living cells in the PAGL group was found to be lowest at $85.85\% \pm 1.72\%$ (Fig. 4b). CCK-8 results (Fig. 4c) indicate that PAGL has a lower OD value on day 3 than other groups, indicating its ability to reduce activity and proliferation rate of HPFs. This may be due to ROS production by AgNPs leading to DNA strand damage resulting in cell death while AL plays an anti-fibrotic role [74–77]. Similar to the results in HUVECs, excess drugs are excreted from the body without causing significant side effects. Cell cycle assays were carried out to analyze the specific causes of cell proliferation inhibition. As shown in Fig. 4d, compared with the normal cell cycle ratio in the BC group, the cell cycle ratio of HPFs treated with PAG, PAL, and PAGL nanofiber films was significantly altered, as evidenced by a decrease in the ratio of the G1 and S phases and a significant increase in the ratio of the G2 phase. Of these, the G2 phase gradually increased from $4.19\% \pm 1.91\%$ in the BC group to $12.31\% \pm 2.73\%$ in the PAG group, $47.80\% \pm 4.45\%$ in the PAL group, and $56.72\% \pm 3.64\%$ in the PAGL group. Thus, PAGL blockades the cell cycle of HPFs in the G2 phase and further inhibit the proliferation of HPFs (Fig. 4e).

A scratch assay verified the antimigration effect of the nanofiber films. As shown in Fig. 4f, the HPFs in the BC group exhibited excellent migration ability as the cell-free gap was nearly closed after 24 h, and the wound closure rate reached $91.63\% \pm 5.22\%$. However, the migrated region of the HPFs gradually decreased in the remaining groups, with the wound closure rate decreasing to $61.65\% \pm 4.56\%$ and $43.01\% \pm 3.18\%$ in the PAG and PAL groups (Fig. 4g), respectively, while the lowest wound closure rate occurred in the PAGL group ($17.97\% \pm 4.99\%$). Overall, PAGL nanofiber film could synergize with AgNPs and AL to exert superior cytotoxicity against HPFs, inhibit the proliferation, and restrain the migration of HPFs, which was beneficial for anti-hyperplasia and subsequent TISR prevention.

Anti-inflammatory coupled anti-angiogenic airway stent prevents TISR in vivo

As shown in Fig. 5a, to validate the potential of the airway stents in preventing TISR, an in vivo airway stent placement was performed in New Zealand rabbits. Figure 5b shows the different airway stents being delivered into the trachea under the guidance of the DSA through the guidewire and stent deliverer. Based on the type of tracheal stents placed, the New Zealand rabbits were divided into four groups: Ctrl, PAG, PAL, and PAGL groups. The procedure time for airway stent placement was similar in all groups; thus, there were no differences in the effects of the different nanofiber film-covered airway stents on the rabbits' respiratory and cardiopulmonary function (Fig. 5e).

Four weeks after stent placement, the tracheal anatomy and stent status were examined using the volume rendering technique (VRT), maximum intensity projection (MIP), and sagittal CT. The airway VRT images depicted varying degrees of tracheal stenosis throughout the stent-covered segment in the Ctrl group and significant stenosis at the ends of the stents in the PAG and PAL groups; only slight airway stenosis occurred in the PAGL group (Fig. 5c). Moreover, stent VRT and MIP images were used to determine the positional relationship between the stent and the surrounding tissue, which showed that all four stent types were securely positioned without any displacement or dislodgment in the airway (Fig. 5d). More importantly, a sagittal CT image (Fig. 5c) showed significant granulation tissue formation and protrusion through the stent into the tracheal lumen in the Ctrl group. The PAG and PAL groups exhibited varying granulation tissue proliferation at both ends of the stent. Interestingly, the PAGL group showed the least granulation tissue formation. Notably, the PAGL group demonstrated the best fit between the airway stent and the trachea compared with the other three groups. An assessment of the tracheal ventilation ratios of the rabbits in each group at

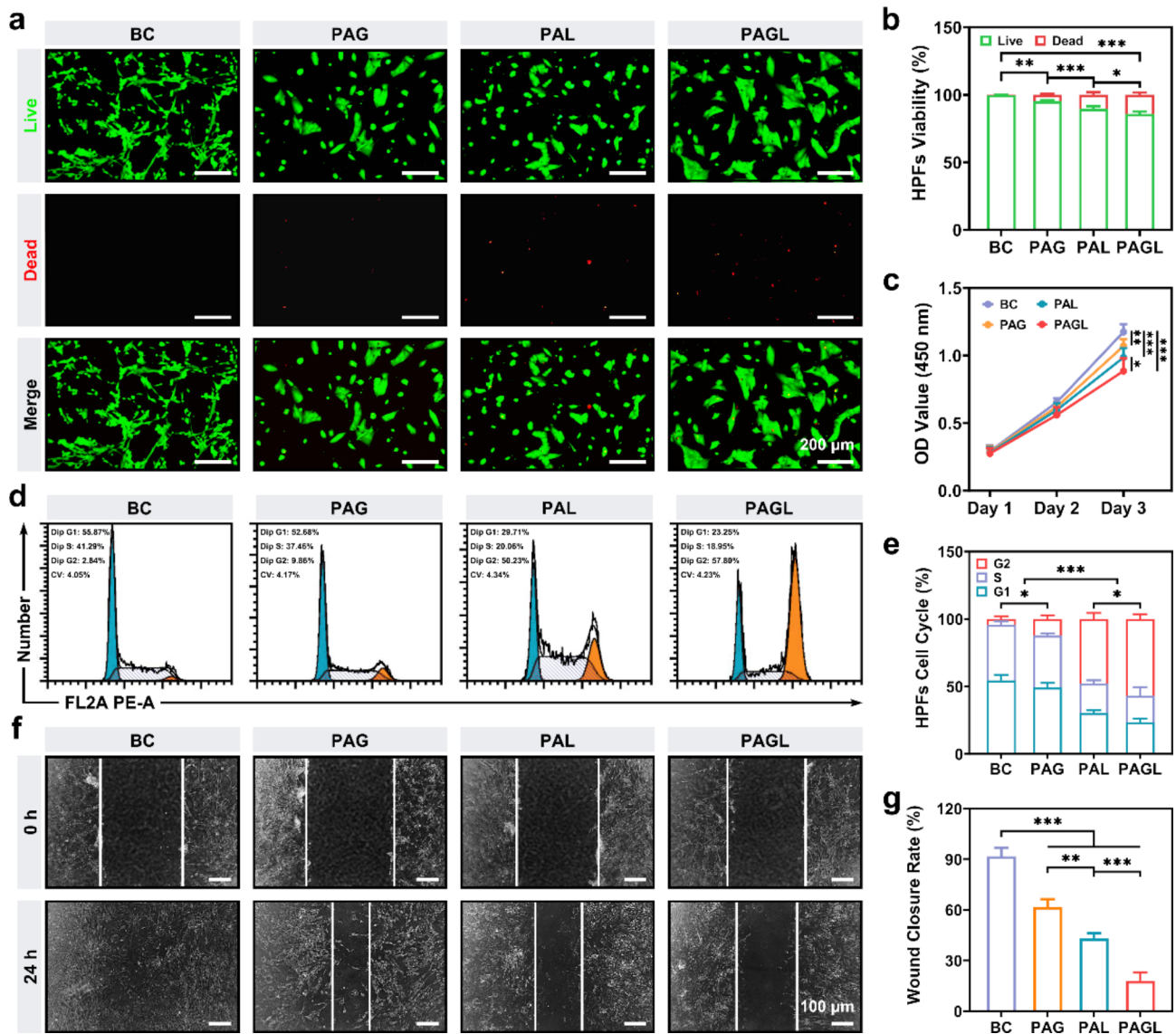


Fig. 4 In vitro anti-hyperplasia of nanofiber films covered on the stent surface. **(a)** Representative live/dead cell staining of HPFs. **(b)** Statistical analysis of HPFs viability. **(c)** Cell proliferation of HPFs over three consecutive days by CCK-8 assay. **(d)** Flow cytometry of cell cycle for HPFs stained with PI. **(e)** Statistical analysis of cell cycle percentage for HPFs. **(f)** Scratch assay of HUVECs. **(g)** Quantitative results of wound closure rate. Scale bar: 100 and 200 μ m. Significant differences: * $P < 0.05$, ** $P < 0.01$, and *** $P < 0.001$

four weeks after stent placement revealed that the tracheal ventilation levels in the remaining three groups were improved compared with those in the Ctrl group, with the PAGL group being the most significant (Fig. 5f).

The tracheal specimens were obtained from the regions proximal and distal to the airway stent. As shown in Fig. 5d, these specimens were subjected to H&E staining and Masson's Trichrome staining to assess TISR progression after airway stent placement. Consistent with CT and reconstructive imaging findings, the Ctrl group exhibited structural damage to the trachea, accompanied by pronounced granulation tissue hyperplasia and extensive collagen deposition. In contrast, the PAGL

group, with its nanofiber-covered stent, displayed an intact tracheal structure with minimal granulation tissue and collagen deposition. Statistical analysis revealed a significant decrease in the epithelial thickness from $742.73 \pm 55.88 \mu$ m in the Ctrl group to $174.29 \pm 18.44 \mu$ m in the PAGL group, indicating marked preservation of the epithelial layer (Fig. 5g). Moreover, a gradual decrease in collagen density appeared, with values ranging from $42.30 \pm 5.98\%$ in the Ctrl group to $34.18 \pm 3.54\%$ in the PAG group, $25.53 \pm 4.44\%$ in the PAL group, and the lowest value of $10.33 \pm 2.49\%$ in the PAGL group (Fig. 5h). The results collectively highlighted the superior

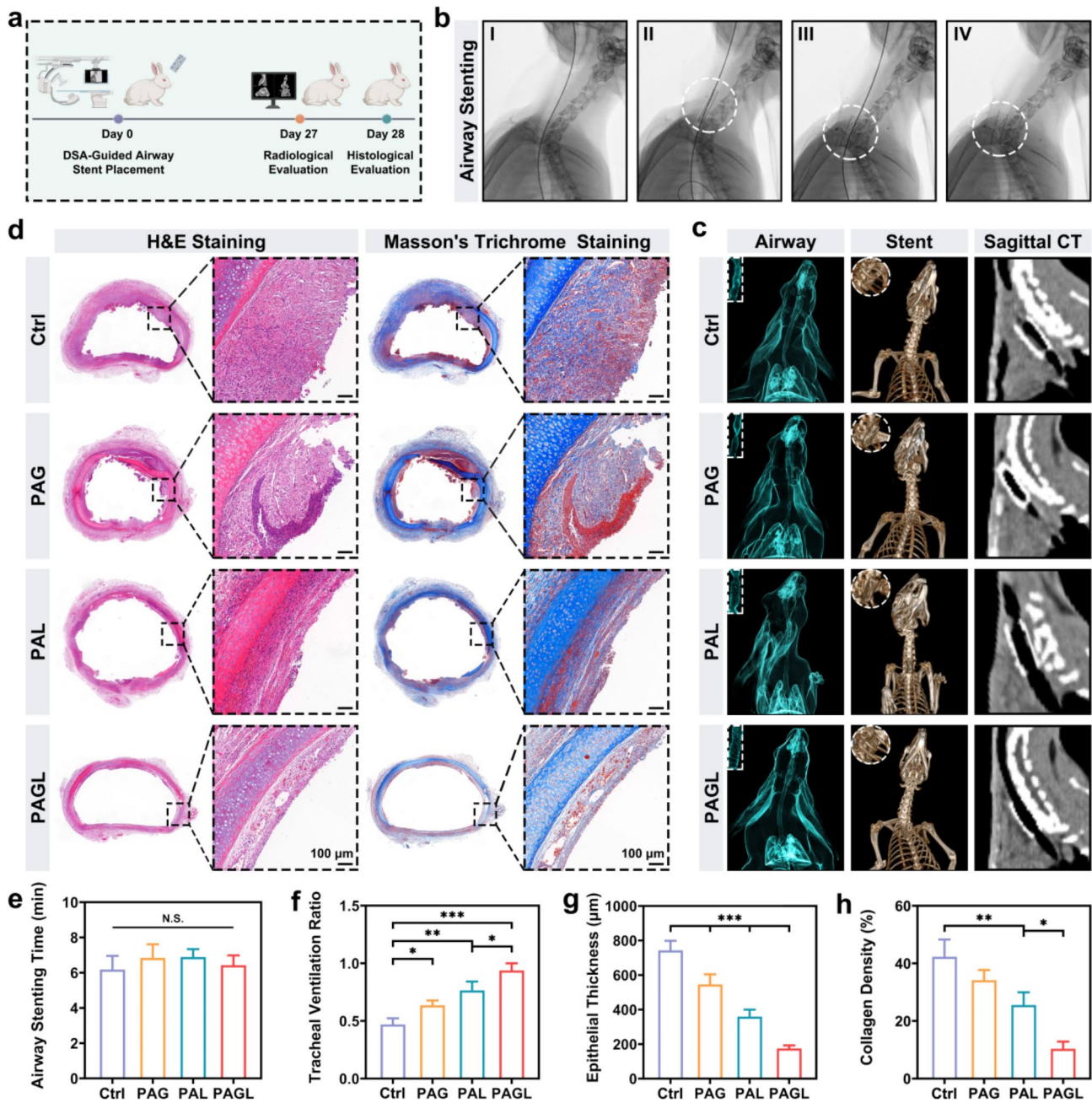


Fig. 5 Airway stent placement and evaluation of postoperative TISR. **(a)** Schematics of the procedural events in the New Zealand rabbit models treated with airway stent placement. **(b)** Diagram of DSA fluoroscopic monitoring images of the airway stent placement procedure in New Zealand rabbits. **(c)** Airway volume rendering technique (VRT) images, stent VRT images, and sagittal CT images four weeks after airway stent placement. **(d)** H&E and Masson's Trichrome staining of the tracheal tissues. **(e)** Airway stenting time for each group. **(f)** Tracheal ventilation ratio in rabbits in each group four weeks after airway stent placement. **(g)** Statistical analysis of tracheal epithelial thickness. **(h)** Statistical analysis of collagen deposition. Scale bar: 100 µm. Significant differences: * $P < 0.05$, ** $P < 0.01$, and *** $P < 0.001$

outcomes achieved by the PAGL group in terms of preventing TISR.

Airway stent suppresses the inflammation response and angiogenesis

Bacterial infection after airway stent placement and chronic inflammatory response resulting from foreign

body irritation are risk factors for TISR [23, 45, 78–80]. To determine the effect of airway stents, film surface microorganisms were collected. The number of viable bacteria was quantified after multiplicative dilution and inoculation onto solid culture substrates. Stents containing AgNPs reduced the microbial content in the airway significantly. The Fig. 6a-b showed the bacterial plate

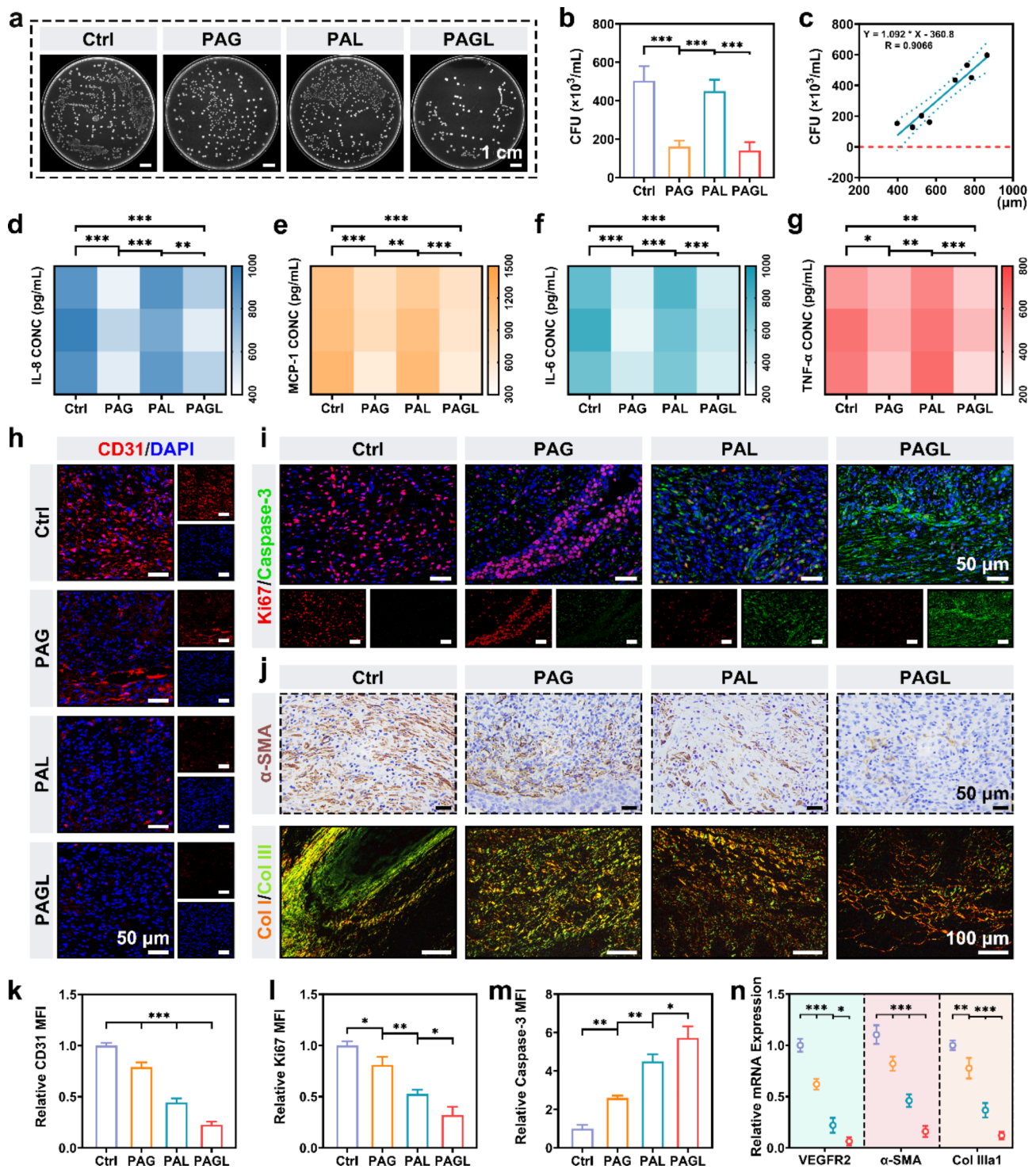


Fig. 6 Airway stent suppresses the inflammation response and angiogenesis. **(a)** Bacterial plate cloning representation of the diluted bacterial contents. **(b)** Statistical analysis of the bacterial contents. **(c)** Correlation analysis of bacterial contents and granuloma formation between the Ctrl and PAG groups. **(d-g)** Expression levels of IL-8, MCP-1, IL-6, and TNF- α in the tracheal tissue. **(h)** Immunofluorescence staining of CD31 in the tracheal tissue. **(i)** Double immunofluorescence staining of Ki67 and Caspase-3 in the tracheal tissue. **(j)** Immunohistochemical staining of α -SMA and Sirius red staining in the tracheal tissue. **(k)** Statistical analysis of relative mean fluorescence intensity (MFI) for CD31. **(l)** Statistical analysis of the relative MFI for Ki67. **(m)** Statistical analysis of the relative MFI for Caspase-3. **(n)** The relative mRNA expression of VEGFR2, α -SMA, and Col IIIa1, respectively. Scale bar: 50 μ m, 100 μ m, and 1 cm. Significant differences: * $P < 0.05$, ** $P < 0.01$, and *** $P < 0.001$

experiments results. Compared with the Ctrl and PAL groups, the surface microbial contents were significantly reduced in the PAG and PAGL groups. The results suggested that AgNPs-containing nanofiber-covered airway stents inhibit the proliferation of microorganisms in the tracheal and maintain the tracheal microecology. In addition, linear regression analysis of the microbial content and the thickness of the tracheal epithelial layer in the Ctrl and PAG groups revealed that the microbial content on the surface of the stent in the tracheal positively correlated with the thickness of the tracheal epithelial layer ($R^2=0.9066$, Fig. 6c). This results confirmed that the higher the microbial content on the stent surface, the more pronounced the granulation tissue hyperplasia in the tracheal. Therefore, by inhibiting the microorganisms in the tracheal and improving the trachea microenvironment, a reduced risk for TISR may be achieved, which will positively improve stent patency.

The levels of inflammatory factors, including IL-8, MCP-1, IL-6, and TNF- α , in the tracheal tissues were quantified using ELISA assay. Based on these factors, IL-8 and MCP-1 are chemokines that recruit inflammatory cells to the local site, where these cells secrete IL-6 and TNF- α , further stimulating fibroblast proliferation and activating vascular endothelial cells [7, 80, 81]. Previous studies have shown that IL-8 and TNF- α are sensitive and specific in detecting early systemic and local inflammatory responses associated with stent-related studies, which may predict the development of TISR after airway stent placement [8, 82]. As depicted in Fig. 6d-g, IL-8, MCP-1, IL-6, and TNF- α were significantly lower in the groups that contained AgNPs (PAG and PAGL groups) compared with the groups without AgNPs (Ctrl and PAL groups). This finding suggests preferred inflammatory control in the PAGL group, aligning with the clinical expectation of airway stents suppressing inflammation.

CD31, a crucial marker of vascular endothelial cells, plays a vital role in early angiogenesis and is commonly used to assess vascularization [83, 84]. Compared with the Ctrl group, CD31 expression was significantly decreased in both the PAG and PAL groups, indicating that both the presence of AgNPs and AL function as inhibitors of angiogenesis in vivo (Fig. 6h). Importantly, CD31 expression was further reduced in the PAGL group, with an approximately 77% decrease in CD31 MFI relative to the Ctrl group (Fig. 6k). The synergistic effect of the combination of AgNPs and AL resulted in the lowest expression of CD31 in the PAGL group, resulting in an enhanced therapeutic effect.

Double immunofluorescence staining for Ki67 and Caspase-3 (Fig. 6i) revealed that tracheal tissues in the Ctrl group exhibited a markedly proliferative state with no signs of apoptosis. With the introduction of AgNPs and/or AL, the relative Ki67 MFI gradually decreased,

and the relative Caspase-3 MFI gradually increased, as observed in the PAG group (0.81 ± 0.08 and 2.58 ± 0.13) and in the PAL group (0.52 ± 0.04 and 4.50 ± 0.38) compared with that in the Ctrl group, respectively. Notably, the relative Ki67 MFI was lowest at 0.32 ± 0.08 , and the relative Caspase-3 MFI was highest at 5.73 ± 0.60 in the PAGL group, respectively (Fig. 6l-m). Highly activated fibroblasts upregulate the expression level of α -SMA expression and secrete excessive collagen I and III, which results in the accumulation of ECM components [7, 85, 86]. To further examine the PAGL's effect on activated fibroblasts, immunohistochemical staining of α -SMA and Sirius red staining of collagen I/III were performed (Fig. 6j). As shown in Fig. S9, the α -SMA positive area in the PAGL group ($1.94\% \pm 0.52\%$) was significantly decreased compared with that in the Ctrl ($20.96\% \pm 2.96\%$), PAG ($13.80\pm 1.30\%$), and PAL ($7.41\% \pm 0.86\%$) groups. Consistent with the findings of MT staining, the Ctrl group exhibited the largest proportion of total collagen, particularly collagen III (green), with the lowest proportion of collagen I/III (Fig. 6j). The increased deposition of collagen III, an immature form of collagen, contributes to the persistent hyperplasia of granulation tissue [87, 88]. Fortunately, the PAGL group demonstrated a significant reduction in the proportion of collagen III and an improvement in the ratio of collagen I/III (Fig. S10). The expression of VEGFR2, α -SMA, and Col IIIa1 mRNA was measured to identify the underlying molecular mechanisms. Figure 6n showed that the PAGL group exhibited the most pronounced inhibitory effect on the expression of molecules associated with angiogenesis and hyperplasia. The results confirm that the PAGL group can reprogram the tracheal microenvironment following stent placement to effectively prevent TISR development by suppressing the inflammatory response and angiogenesis.

Whole blood samples were collected from each group of New Zealand rabbits to assess liver and kidney function at four weeks. There were no significant differences in liver and kidney function indicators (e.g., albumin, alanine aminotransferase, aspartate aminotransferase, total bilirubin, blood urea nitrogen, and creatinine) among the groups (Fig. S11). This result confirms the excellent biocompatibility of the PAGL nanofiber-covered airway stent.

RNA sequencing analysis of the therapeutic performance of PAGL

Following in vitro and in vivo validation, RNA sequencing was conducted to elucidate the molecular mechanism underlying PAGL treatment of the tracheal tissue. As depicted in Fig. 7a, differential analysis revealed significant upregulation of 24 genes and downregulation of 194 genes. Notably, several highly expressed genes in the Ctrl

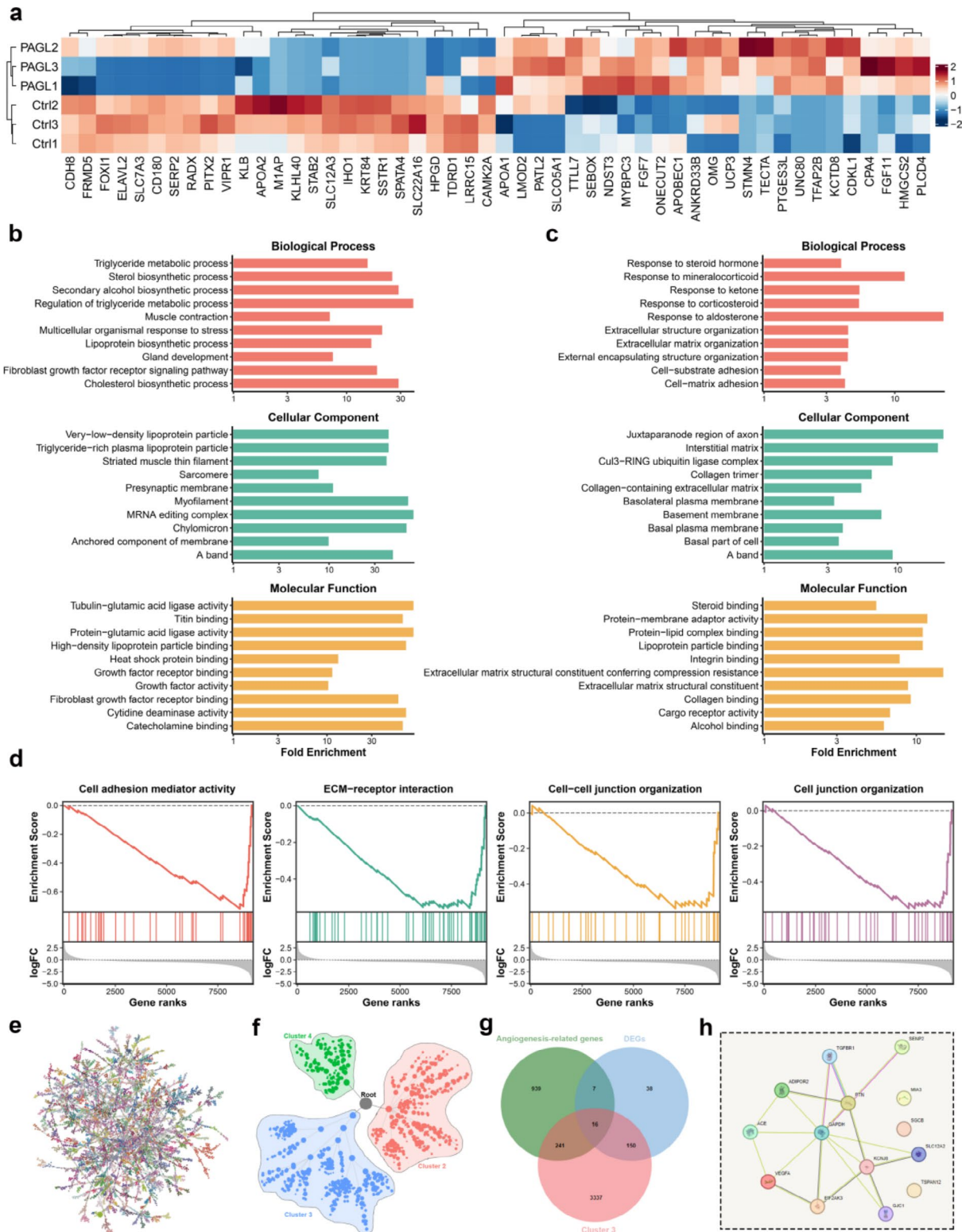


Fig. 7 Biological function analysis of PAGL treatment. **(a)** A heatmap illustrating the differentially expressed genes (DEGs) identified in the PAGL and Ctrl groups ($n = 3$). **(b-c)** Gene Ontology enrichment analysis of the identified DEGs in the Ctrl and PAGL groups, respectively. **(d)** Gene Set Enrichment Analysis results are based on the fold-change in gene expression between the PAGL and Ctrl groups. **(e)** Multiscale embedded gene co-expression network analysis. **(f)** Three clusters were obtained using MEGENAR package. **(g)** Overlap of cluster 3 genes with DEGs and Angiogenesis-related genes. Sixteen genes: SIRT1, OVOL2, VEGFA, TSPAN12, EIF2AK3, KCNJ8, GJC1, MIA3, SENP2, ADIPOR2, SLC12A2, SGCB, PTN, ACE, GAPDH, and TGFBR1. **(h)** Protein-protein interaction analysis

group, including FOXI1, ELAVL2, and SLC7A3, were closely associated with fibrosis, intimal hyperplasia, and cell migration [89–91]. To further investigate the potential biological functions of these differentially expressed genes (DEGs), enrichment analysis based on Gene Ontology gene sets demonstrated their involvement in pathways associated with ECM remodeling and emergency response (Fig. 7b–c). In addition, Gene Set Enrichment Analysis indicated a negative correlation between the PAGL group and cell adhesion (Fig. 7d). Furthermore, we conducted Multiscale embedded gene co-expression network analysis for all genes (Fig. 7e), resulting in the identification of three distinct clusters (Fig. 7f). The results of GO enrichment analysis (Fig. S12) revealed that cluster 3 was primarily associated with angiogenesis, while immune-related functions, particularly antigen processing and presentation, were also significantly enriched. Subsequently, we compared gene cluster 3 with DEGs and angiogenesis-related genes, leading to the discovery of 16 closely related genes involved in angiogenesis after PAGL treatment within cluster 3, including SIRT1, MIA3, SENP2, ADIPOR2, SLC12A2, TGFBR1 and other genes (Fig. 7g). The results of PPI analysis using string database show that there are interactions among GAPDH, VEGFA, TGFBR1 and other proteins (Fig. 7h). These findings suggest their potential involvement in the regulation of anti-angiogenesis processes and effective inhibition of in-stent restenosis. Similarly, through the integration of gene cluster 3 with DEGs and immune-related genes, we have identified a potential involvement of 12 genes in cluster 3 in regulating the immune response following PAGL treatment. Furthermore, analysis of PPI results has revealed interactions between CTSC, PLA2G4A, PTN and MME (Fig. S13). In summary, the primary function of PAGL is to suppress angiogenesis, regulate immune response, exert an anti-inflammatory role, effectively inhibit granulation tissue proliferation and fibrosis formation, thereby inhibiting in-stents restenosis.

Discussion

TISR is an outcome event following an abnormal tracheal microenvironment triggered by the foreign body reaction of airway stents. It is granulation tissue hyperplasia's most prominent pathological hallmark [17]. In recent years, studies on drug-eluting stents have used cytotoxic drugs, such as paclitaxel, rapamycin, mitomycin, and cisplatin, to inhibit granulation tissue hyperplasia by counteracting fibroblast proliferation [45, 92–94]. For example, Wang et al. reported that paclitaxel-eluting stents could be safely placed in vivo and reduced granulation tissue formation [92]. Moreover, Duvvuri et al. designed rapamycin-eluting airway stents to effectively inhibit fibroblast proliferation and collagen deposition [93]. However, excessive inflammation and vascularization are also crucial factors

contributing to TISR [7, 17]. Thus, compared with the studies above, PAGL nanofiber-covered airway stents in the present study alleviate the inflammatory response and suppress uncontrolled vascularization by synergizing AgNPs and AL.

The controlled release of active molecules from biomaterials represents one approach to modulating inflammation at the implant site. Choi et al. reported that a nitinol stent coated with doxycycline positively reduced tracheal inflammation and restenosis in a rabbit model [22]. Moreover, stent-associated bacterial infections, particularly MRSA, further exacerbate the inflammatory response and subsequent granulation tissue hyperplasia. Two clinical studies described the correlation between granulation tissue formation and airway microbial colonization after airway stent placement [95, 96]. Thus, Zhao et al. investigated the efficacy of vancomycin-loaded nanofiber-covered airway stents in reducing granulation tissue hyperplasia by inhibiting bacterial infection and inflammatory response [38]. In a preliminary study, AgNPs were combined with PAGL nanofiber-covered airway stents to exert antimicrobial and anti-inflammatory effects. The present study also confirmed that compared with the groups without AgNPs (PLA and PAL groups), the groups containing AgNPs (PAG and PAGL groups) not only effectively inactivated MRSA by generating ROS and inducing protein leakage (Fig. 2), but also downregulated the expression of IL-8, MCP-1, IL-6, and TNF- α (Fig. 6d–g). These results indicate that PAGL nanofiber-covered airway stents inhibit bacterial infection and alleviate the inflammatory response during development of TISR.

Compared with previously designed functionalized airway stents with anti-inflammatory and/or anti-proliferative activity, the present study innovatively proposes to target uncontrolled angiogenesis, another pivotal event in developing granulation tissue hyperplasia. We also confirmed that PAGL nanofiber film not only inhibits the viability, proliferation, and migration of HUVECs and HPFs in vitro (Figs. 3 and 4), but also inhibits the expression of VEGFR and suppresses angiogenesis in vivo (Fig. 6k). Notably, the PAL nanofiber-covered airway stent loaded with AL alone was effective at preventing TISR by simply inhibiting angiogenesis, which provides a theoretical basis for the feasibility of the anti-angiogenesis strategy in addressing TISR. Moreover, PAG nanofiber films loaded with AgNPs alone also exhibit modest anti-angiogenic and anti-proliferative effects; however, further analysis of the PAL, PAG and PAGL groups revealed that the anti-angiogenic effect of the PAGL nanofiber film was primarily due to AL, which is consistent with previous pharmacological studies [38–40]. It is noteworthy that the majority of released AgNPs and AL primarily target granulation tissue. As animals function as complete

biological systems, a minimal amount of unused drugs are continuously excreted through metabolic processes, thereby minimizing harm to the body. Consequently, in future clinical practice, it is imperative to strictly administer the appropriate drug concentration via stents based on individual patient's disease condition to achieve optimal therapeutic outcomes.

The unique spatial structure and good biocompatibility of electrospun nanofiber films in combination with conventional SEMS may be used to develop multifunctional drug-loaded nanofiber-covered airway stents. In our preliminary work, we focused on the anatomical structure of the trachea and developed a series of SEMS (named Han's stent), which solved the problem of accurate fitting of the stent and the trachea. Next, we use polylactic acid as an electrospinning drug carrier, which has been approved by the US Food and Drug Administration (FDA) for medical device applications, to explore nanofiber-covered airway stent based on SEMS [97]. Nanofiber films have the following advantages: (1) similarity to the three-dimensional structure of the ECM can provide effective mechanical support for cells [98, 99]; (2) a large specific surface area and porous structure is favorable to the loading of a variety of drugs and can achieve high concentrations of drug-release at the target site [100, 101]; and (3) the electrospinning fabrication process is convenient, versatile, and cost effective [102]. This study lays the groundwork for future personalized therapy by highlighting the biocompatibility and modifiability of electrospun nanofiber-covered airway stents, which may be modified with various drugs or nanomaterials.

In summary, we successfully fabricated a new PAGL nanofiber-covered airway stent with anti-inflammatory coupled anti-angiogenic properties using electrospinning technology. The PAGL nanofiber film, dual-loaded with AgNPs and AL exhibited excellent mechanical properties and a sustained, controlled drug-release profile. In vitro experiments indicated that the PAGL nanofiber film could effectively combat MRSA because of the bactericidal properties of AgNPs. It also inhibited the viability, proliferation, and migration of HUVECs and HPFs synergistically with AgNPs and AL. Subsequently, airway stent placement in a New Zealand rabbit model demonstrated that the PAGL nanofiber-covered airway stent effectively alleviated inflammation and suppressed vascularization, thereby reducing collagen deposition and preventing granulation tissue hyperplasia. Finally, the favorable biosafety and biocompatibility of the PAGL nanofiber-covered airway stent were evaluated. This innovative airway stent may prevent TISR and enhance clinical outcomes.

Supplementary Information

The online version contains supplementary material available at <https://doi.org/10.1186/s12951-024-03087-y>.

Supplementary Material 1

Acknowledgements

The authors thank Prof. Yun Chen from Wuhan University for the great support. We thank Center of Advanced Analysis & Gene Sequencing, Zhengzhou University and Laboratory Animal Center, Zhengzhou University for the equipment support. We thank Academy of Medical Sciences of Zhengzhou University Translational Medicine platform.

Author contributions

Yanan Zhao, Yong Jiang and Xinwei Han designed the experiments. Yiming Liu and Jiheng Shan performed the synthesis and characterization of the materials. Xiaohong Xu, Zhaoqian Zhong, Yanxia Gao and Zaoqu Liu participated in the in vivo experiments. Chengzhi Zhang, Xiaomeng Li and Kewei Ren contributed to data analysis. Dechao Jiao, Jianzhuang Ren, Ping Wu and Yanan Zhao contributed to the manuscript preparation. All authors read and approved the final manuscript.

Funding

This work was supported by National Natural Science Foundation of China (82302328), Henan Province Youth and Middle-aged Health Science and Technology Innovation Excellent Youth Talent Training Program (YQRC2024014), and Major Science and Technology Special Project of Henan Province (221100310100).

Data availability

No datasets were generated or analysed during the current study.

Declarations

Ethics approval and consent to participate

All animal experiments were granted approval by the animal care committee of the First Affiliated Hospital of Zhengzhou University (2023042602).

Consent for publication

Written informed consent for publication was obtained from all participants.

Competing interests

The authors declare no competing interests.

Received: 3 July 2024 / Accepted: 29 December 2024

Published online: 29 January 2025

References

1. Guibert N, Saka H, Dutau H. Airway stenting: Technological advancements and its role in interventional pulmonology. *Respirology*. 2020;25:953–62.
2. Murgu SD, Egressy K, Laxmanan B, Doblare G, Ortiz-Comino R, Hogarth DK. Central Airway obstruction: Benign strictures, Tracheobronchomalacia, and malignancy-related obstruction. *Chest*. 2016;150:426–41.
3. Li L, Zhang X, Shi J, Chen Y, Wan H, Herth FJ, Luo F. Airway stents from now to the future: a narrative review. *Respiration*. 2023;102:439–48.
4. Avsarala SK, Freitag L, Mehta AC. Metallic endobronchial stents: a contemporary resurrection. *Chest*. 2019;155:1246–59.
5. Lin L-Q, Chen D-F, Wu H-K, Chen Y, Zhong C-H, Chen X-B, Tang C-L, Zhou Z-Q, Li S-Y. Long-term efficacy and safety of the Dumon stent for treatment of benign airway stenosis. *Ther Adv Respir Dis* 2023, 17.
6. Tian S, Huang H, Hu Z, Dong Y, Bai C. A narrative review of progress in airway stents. *J Thorac Disease*. 2022;14:1674–83.
7. Zhang D, Chen Q, Shi C, Chen M, Ma K, Wan J, Liu R. Dealing with the Foreign-Body response to implanted biomaterials: strategies and applications of new materials. *Adv Funct Mater* 2020, 31.
8. Arellano-Orden E, Serrano C, Montes-Worboys A, Sánchez-López V, Laborda A, Lostalé F, Lahuerta C, Rodríguez-Panadero F, de Gregorio M. Stent-induced tracheal stenosis can be predicted by IL-8 expression in rabbits. *Eur J Clin Invest*. 2017;47:84–92.
9. Yang Y, Gao P, Wang J, Tu Q, Bai L, Xiong K, Qiu H, Zhao X, Maitz MF, Wang H et al. Endothelium-Mimicking Multifunctional Coating Modified Cardiovascular

- Stents via a Stepwise Metal-Catechol-(Amine) Surface Engineering Strategy. *Research* 2020, 2020.
10. Vasconcelos DP, Águas AP, Barbosa MA, Pelegrín P, Barbosa JN. The inflammatory response in host response to biomaterials: bridging inflammation and tissue regeneration. *Acta Biomater.* 2019;83:1–12.
 11. Anderson JM, Rodriguez A, Chang DT. Foreign body reaction to biomaterials. *Semin Immunol.* 2008;20:86–100.
 12. Klopffleisch R, Jung F. The pathology of the foreign body reaction against biomaterials. *J Biomed Mater Res A.* 2017;105:927–40.
 13. Zhou G, Groth T. Host responses to Biomaterials and Anti-inflammatory Design—a brief review. *Macromol Biosci.* 2018;18:e1800112.
 14. Zhang M, Chen H, Qian H, Wang C. Characterization of the skin keloid micro-environment. *Cell Commun Signal.* 2023;21:207.
 15. Kumar AS, Kamalasanan K. Drug delivery to optimize angiogenesis imbalance in keloid: a review. *J Control Release.* 2021;329:1066–76.
 16. Selders GS, Fetz AE, Radic MZ, Bowlin GL. An overview of the role of neutrophils in innate immunity, inflammation and host-biomaterial integration. *Regen Biomater.* 2017;4:55–68.
 17. Roodenburg SA, Pouwels SD, Slobes D-J. Airway granulation response to lung-implantable medical devices: a concise overview. *Eur Respiratory Rev* 2021, 30.
 18. Ost DE, Shah AM, Lei X, Godoy MCB, Jimenez CA, Eapen GA, Jani P, Larson AJ, Sarkiss MG, Morice RC. Respiratory infections increase the risk of granulation tissue formation following airway stenting in patients with malignant airway obstruction. *Chest.* 2012;141:1473–81.
 19. Heo DN, Lee JB, Bae MS, Hwang YS, Kwon KH, Kwon IK. Development of nanofiber coated indomethacin-eluting stent for tracheal regeneration. *J Nanosci Nanotechnol.* 2011;11:5711–6.
 20. Shin JH, Song HY, Seo TS, Yuk SH, Kim YH, Cho YM, Choi GB, Kim TH, Suh JY. Influence of a dexamethasone-eluting covered stent on tissue reaction: an experimental study in a canine bronchial model. *Eur Radiol.* 2005;15:1241–9.
 21. Baskaran R, Ko UJ, Davaa E, Park JE, Jiang Y, Lee J, Yang SG. Doxycycline-Eluting Core-Shell Type Nanofiber-Covered Trachea Stent for Inhibition of Cellular Metalloproteinase and Its Related Fibrotic Stenosis. *Pharmaceutics* 2019, 11.
 22. Choi JS, Kim JM, Kim JW, Kim YM, Park IS, Yang SG. Prevention of tracheal inflammation and fibrosis using nitinol stent coated with doxycycline. *Laryngoscope.* 2018;128:1558–63.
 23. Zhao Y, Tian C, Wu K, Zhou X, Feng K, Li Z, Wang Z, Han X. Vancomycin-Loaded Polycaprolactone Electrospinning nanofibers modulate the Airway Interfaces to restrain tracheal stenosis. *Front Bioeng Biotechnol* 2021, 9.
 24. Morozova OV. Silver nanostructures: limited sensitivity of detection, toxicity and Anti-inflammation effects. *Int J Mol Sci* 2021, 22.
 25. Tang S, Zheng J. Antibacterial activity of silver nanoparticles: Structural effects. *Adv Healthc Mater.* 2018;7:e1701503.
 26. Xu L, Wang YY, Huang J, Chen CY, Wang ZX, Xie H. Silver nanoparticles: synthesis, medical applications and biosafety. *Theranostics.* 2020;10:8996–9031.
 27. Parnsamut C, Brimson S. Effects of silver nanoparticles and gold nanoparticles on IL-2, IL-6, and TNF- α production via MAPK pathway in leukemic cell lines. *Genet Mol Res.* 2015;14:3650–68.
 28. Zhang J, Li Q, Bai C, Han Y, Huang Y. Inhalation of TGF- β 1 antibody: a new method to inhibit the airway stenosis induced by the endobronchial tuberculosis. *Med Hypotheses.* 2009;73:1065–6.
 29. Csermely P, Agoston V, Pongor S. The efficiency of multi-target drugs: the network approach might help drug design. *Trends Pharmacol Sci.* 2005;26:178–82.
 30. Gurusamy M, Nasser S, Rampa DR, Feng H, Lee D, Pekcec A, Doods H, Wu D. Triple-tyrosine kinase inhibition by BIBF1000 attenuates airway and pulmonary arterial remodeling following chronic allergen challenges in mice. *Eur J Med Res.* 2023;28:71.
 31. Zhou BY, Wang WB, Wu XL, Zhang WJ, Zhou GD, Gao Z, Liu W. Nintedanib inhibits keloid fibroblast functions by blocking the phosphorylation of multiple kinases and enhancing receptor internalization. *Acta Pharmacol Sin.* 2020;41:1234–45.
 32. Li G, Han Q, Lu P, Zhang L, Zhang Y, Chen S, Zhang P, Zhang L, Cui W, Wang H, Zhang H. Construction of Dual-Biofunctionalized Chitosan/Collagen Scaffolds for Simultaneous Neovascularization and Nerve Regeneration. *Research* 2020, 2020.
 33. Sun L, Fan L, Bian F, Chen G, Wang Y, Zhao Y. MXene-Integrated Microneedle Patches with Innate Molecule Encapsulation for Wound Healing. *Research* 2021, 2021.
 34. Ding X, Yu Y, Yang C, Wu D, Zhao Y. Multifunctional GO Hybrid Hydrogel scaffolds for Wound Healing. *Research.* 2022;2022:1–14.
 35. Ding X, Zhang W, Xu P, Feng W, Tang X, Yang X, Wang L, Li L, Huang Y, Ji J et al. The Regulatory Effect of Braided Silk Fiber Skeletons with Differential Porosities on In Vivo Vascular Tissue Regeneration and Long-Term Patency. *Research* 2022, 2022.
 36. Wu Z, Zhuang H, Ma B, Xiao Y, Koc B, Zhu Y, Wu C. Manganese-Doped Calcium Silicate Nanowire Composite Hydrogels for Melanoma Treatment and Wound Healing. *Research* 2021, 2021.
 37. Chen W, di Carlo C, Devery D, McGrath DJ, McHugh PE, Kleinsteinberg K, Jockenhoewel S, Hennink WE, Kok RJ. Fabrication and characterization of gefitinib-releasing polyurethane foam as a coating for drug-eluting stent in the treatment of bronchotracheal cancer. *Int J Pharm.* 2018;548:803–11.
 38. Shen G, Zheng F, Ren D, Du F, Dong Q, Wang Z, Zhao F, Ahmad R, Zhao J. Anlotinib: a novel multi-targeting tyrosine kinase inhibitor in clinical development. *J Hematol Oncol* 2018, 11.
 39. Ruan H, Lv Z, Liu S, Zhang L, Huang K, Gao S, Gan W, Liu X, Zhang S, Helian K, et al. Anlotinib attenuated bleomycin-induced pulmonary fibrosis via the TGF- β 1 signalling pathway. *J Pharm Pharmacol.* 2020;72:44–55.
 40. Lei J, Li Q, Xu H, Luo M, Liu Z, Xiang D, Chen P. Anlotinib improves bile duct ligature-induced liver fibrosis in rats via antiangiogenesis regulated by VEGFR2/mTOR pathway. *Drug Dev Res.* 2023;84:143–55.
 41. Li L, Hao R, Qin J, Song J, Chen X, Rao F, Zhai J, Zhao Y, Zhang L, Xue J. Electrospun fibers Control Drug Delivery for tissue regeneration and Cancer therapy. *Adv Fiber Mater.* 2022;4:1375–413.
 42. Wan X, Zhao Y, Li Z, Li L. Emerging polymeric electrospun fibers: from structural diversity to application in flexible bioelectronics and tissue engineering. *Exploration* 2022, 2.
 43. Xia G, Song B, Fang J. Electrical Stimulation Enabled via Electrospun Piezoelectric Polymeric Nanofibers for Tissue Regeneration. *Research* 2022, 2022.
 44. Li Y, Li M, Wang X, Wang Y, Li C, Zhao Y, Li Z, Chen J, Li J, Ren K, et al. Arsenic trioxide-eluting electrospun nanofiber-covered self-expandable metallic stent reduces granulation tissue hyperplasia in rabbit trachea. *Biomed Mater.* 2020;16:015013.
 45. Li Z, Tian C, Jiao D, Li J, Li Y, Zhou X, Zhao H, Zhao Y, Han X. Synergistic effects of silver nanoparticles and cisplatin in combating inflammation and hyperplasia of airway stents. *Bioactive Mater.* 2022;9:266–80.
 46. Zhao Y, Liu Y, Liu Z, Ren K, Jiao D, Ren J, Wu P, Li X, Wang Z, Han X. In situ nanofiber Patch boosts postoperative Hepatocellular Carcinoma Immune activation by Trimodal Combination Therapy. *ACS Nano.* 2024;18:245–63.
 47. Seyhan SA, Alkaya DB, Cesur S, Sahin A. Investigation of the antitumor effect on breast cancer cells of the electrospun amygdalin-loaded poly(L-lactic acid)/poly(ethylene glycol) nanofibers. *Int J Biol Macromol.* 2023;239:124201.
 48. Liu Y, Tian C, Zhang C, Liu Z, Li J, Li Y, Zhang Q, Ma S, Jiao D, Han X, Zhao Y. One-stop synergistic strategy for hepatocellular carcinoma postoperative recurrence. *Mater Today Bio.* 2023;22:100746.
 49. Liu W, Lipner J, Moran CH, Feng L, Li X, Thomopoulos S, Xia Y. Generation of electrospun nanofibers with controllable degrees of crimping through a simple, plasticizer-based treatment. *Adv Mater.* 2015;27:2583–8.
 50. Lin CC, Fu SJ, Lin YC, Yang IK, Gu Y. Chitosan-coated electrospun PLA fibers for rapid mineralization of calcium phosphate. *Int J Biol Macromol.* 2014;68:39–47.
 51. Yataka Y, Suzuki A, Iijima K, Hashizume M. Enhancement of the mechanical properties of polysaccharide composite films utilizing cellulose nanofibers. *Polym J.* 2020;52:645–53.
 52. Huang Y, Song J, Yang C, Long Y, Wu H. Scalable manufacturing and applications of nanofibers. *Mater Today.* 2019;28:98–113.
 53. Chen X, Cao H, He Y, Zhou Q, Li Z, Wang W, He Y, Tao G, Hou C. Advanced functional nanofibers: strategies to improve performance and expand functions. *Front Optoelectron* 2022, 15.
 54. Kumar G, Engle K. Natural products acting against *S. Aureus* through membrane and cell wall disruption. *Nat Prod Rep.* 2023;40:1608–46.
 55. Lakhundi S, Zhang K. Methicillin-Resistant *Staphylococcus aureus*: molecular characterization, evolution, and Epidemiology. *Clin Microbiol Rev* 2018, 31.
 56. Dondossola E, Holzapfel BM, Alexander S, Filippini S, Hutmacher DW, Friedl P. Examination of the foreign body response to biomaterials by nonlinear intravital microscopy. *Nat Biomed Eng* 2016, 1.
 57. Zhang L, Cao Z, Bai T, Carr L, Ella-Menye JR, Irvin C, Ratner BD, Jiang S. Zwitterionic hydrogels implanted in mice resist the foreign-body reaction. *Nat Biotechnol.* 2013;31:553–6.
 58. Wang X, Yang C, Yu Y, Zhao Y. In Situ 3D Bioprinting Living Photosynthetic Scaffolds for Autotrophic Wound Healing. *Research* 2022, 2022.
 59. He J, Ma Y, Niu X, Pei J, Yan R, Xu F, Ma J, Ma X, Jia S, Ma W. Silver nanoparticles induce endothelial cytotoxicity through ROS-mediated

- mitochondria-lysosome damage and autophagy perturbation: the protective role of N-acetylcysteine. *Toxicology*. 2024;502:153734.
60. Shi J, Sun X, Lin Y, Zou X, Li Z, Liao Y, Du M, Zhang H. Endothelial cell injury and dysfunction induced by silver nanoparticles through oxidative stress via IKK/NF- κ B pathways. *Biomaterials*. 2014;35:6657–66.
61. Shen G, Zheng F, Ren D, Du F, Dong Q, Wang Z, Zhao F, Ahmad R, Zhao J. Anlotinib: a novel multi-targeting tyrosine kinase inhibitor in clinical development. *J Hematol Oncol*. 2018;11:120.
62. Zhen Z, Xiang L, Li S, Li H, Lei Y, Chen W, Jin JM, Liang C, Tang SY. Designing a whole-cell biosensor applicable for S-adenosyl-L-methionine-dependent methyltransferases. *Biosens Bioelectron*. 2025;268:116904.
63. Wu J, Zhang S, Yu S, An G, Wang Y, Yu Y, Liang L, Wang Y, Xu X, Xiong Y, et al. Nivolumab plus anlotinib hydrochloride in advanced gastric adenocarcinoma and esophageal squamous cell carcinoma: the phase II OASIS trial. *Nat Commun*. 2024;15:8876.
64. Nagy JA, Dvorak AM, Dvorak HF. VEGF-A and the induction of pathological angiogenesis. *Annu Rev Pathol*. 2007;2:251–75.
65. Cao Y, Langer R, Ferrara N. Targeting angiogenesis in oncology, ophthalmology and beyond. *Nat Rev Drug Discov*. 2023;22:476–95.
66. Ferrara N, Adamis AP. Ten years of anti-vascular endothelial growth factor therapy. *Nat Rev Drug Discov*. 2016;15:385–403.
67. Limaverde-Sousa G, Sternberg C, Ferreira CG. Antiangiogenesis beyond VEGF inhibition: a journey from antiangiogenic single-target to broad-spectrum agents. *Cancer Treat Rev*. 2014;40:548–57.
68. Lin B, Song X, Yang D, Bai D, Yao Y, Lu N. Anlotinib inhibits angiogenesis via suppressing the activation of VEGFR2, PDGFR β and FGFR1. *Gene*. 2018;654:77–86.
69. Yang Q, Ni L, Imani S, Xiang Z, Hai R, Ding R, Fu S, Wu Jb, Wen Q. Anlotinib suppresses Colorectal Cancer Proliferation and Angiogenesis via Inhibition of AKT/ERK Signaling Cascade. *Cancer Manage Res*. 2020;12:4937–48.
70. Gurunathan S, Lee KJ, Kalishwaralal K, Sheikpranbabu S, Vaidyanathan R, Eom SH. Antiangiogenic properties of silver nanoparticles. *Biomaterials*. 2009;30:6341–50.
71. Jang S, Park JW, Cha HR, Jung SY, Lee JE, Jung SS, Kim JO, Kim SY, Lee CS, Park HS. Silver nanoparticles modify VEGF signaling pathway and mucus hypersecretion in allergic airway inflammation. *Int J Nanomed*. 2012;7:1329–43.
72. Kalishwaralal K, Banumathi E, Ram Kumar Pandian S, Deepak V, Muniyandi J, Eom SH, Gurunathan S. Silver nanoparticles inhibit VEGF induced cell proliferation and migration in bovine retinal endothelial cells. *Colloids Surf B Biointerfaces*. 2009;73:51–7.
73. Wang Z, Zhao H, Tang X, Meng T, Khutsishvili D, Xu B, Ma S. CNS Organoid Surpasses Cell-Laden Microgel Assembly to Promote Spinal Cord Injury Repair. *Research*. 2022, 2022.
74. Klabusay M, Skopalík J, Erceg S, Hrdlička A. Aequorin as intracellular Ca²⁺ indicator incorporated in follicular lymphoma cells by hypoosmotic shock treatment. *Folia Biol (Praha)*. 2015;61:134–9.
75. Wang Y, Li H, Xue C, Chen H, Xue Y, Zhao F, Zhu MX, Cao Z. TRPV3 enhances skin keratinocyte proliferation through EGFR-dependent signaling pathways. *Cell Biol Toxicol*. 2021;37:313–30.
76. Chen W, Zhang J, Zhong W, Liu Y, Lu Y, Zeng Z, Huang H, Wan X, Meng X, Zou F, et al. Anlotinib inhibits PFKFB3-Driven glycolysis in Myofibroblasts to reverse pulmonary fibrosis. *Front Pharmacol*. 2021;12:744826.
77. Xiong Y, Xu X, Zhou X, Tong Y, Yu C. Anlotinib inhibits cervical cancer cell proliferation and invasion by suppressing cytokine secretion in activated cancer-associated fibroblasts. *Front Oncol*. 2024;14:1412660.
78. Chandorkar Y, K R, Basu B. The foreign body response demystified. *ACS Biomater Sci Eng*. 2019;5:19–44.
79. Chu C, Liu L, Rung S, Wang Y, Ma Y, Hu C, Zhao X, Man Y, Qu Y. Modulation of foreign body reaction and macrophage phenotypes concerning microenvironment. *J Biomed Mater Res A*. 2020;108:127–35.
80. Veisoh O, Vegas AJ. Domesticating the foreign body response: recent advances and applications. *Adv Drug Deliv Rev*. 2019;144:148–61.
81. Shi C, Pamer EG. Monocyte recruitment during infection and inflammation. *Nat Rev Immunol*. 2011;11:762–74.
82. Wei P, Huang Z, Gan L, Li Y, Qin C, Liu G. Nintedanib ameliorates tracheal stenosis by activating HDAC2 and suppressing IL-8 and VEGF in rabbit. *Am J Transl Res*. 2020;12:4739–48.
83. Daido W, Nakashima T, Masuda T, Sakamoto S, Yamaguchi K, Horimasu Y, Miyamoto S, Iwamoto H, Fujitaka K, Hamada H, Hattori N. Nestin and Notch3 collaboratively regulate angiogenesis, collagen production, and endothelial-mesenchymal transition in lung endothelial cells. *Cell Commun Signal*. 2023;21:247.
84. Zhang Y, He F, Zhang Q, Lu H, Yan S, Shi X. 3D-Printed flat-bone-mimetic bioceramic scaffolds for cranial restoration. *Research*. 2023, 6.
85. Ehrlich HP, Desmoulière A, Diegelmann RF, Cohen IK, Compton CC, Garner WL, Kapanci Y, Gabbiani G. Morphological and immunochemical differences between keloid and hypertrophic scar. *Am J Pathol*. 1994;145:105–13.
86. Shook BA, Wasko RR, Rivera-Gonzalez GC, Salazar-Gatzimas E, López-Giráldez F, Dash BC, Muñoz-Rojas AR, Aultman KD, Zwick RK, Lei V, et al. Myofibroblast proliferation and heterogeneity are supported by macrophages during skin repair. *Science*. 2018, 362.
87. Singh D, Rai V, Agrawal DK. Regulation of collagen I and Collagen III in tissue Injury and Regeneration. *Cardiol Cardiovasc Med*. 2023;7:5–16.
88. Mathew-Steiner SS, Roy S, Sen CK. Collagen in Wound Healing. *Bioeng (Basel)*. 2021, 8.
89. Plasschaert LW, Žilionis R, Choo-Wing R, Savova V, Knehr J, Roma G, Klein AM, Jaffe AB. A single-cell atlas of the airway epithelium reveals the CFTR-rich pulmonary ionocyte. *Nature*. 2018;560:377–81.
90. Montoro DT, Haber AL, Biton M, Vinarsky V, Lin B, Birket SE, Yuan F, Chen S, Leung HM, Villoria J, et al. A revised airway epithelial hierarchy includes CFTR-expressing ionocytes. *Nature*. 2018;560:319–24.
91. Wang P, Song Y, Li H, Zhuang J, Shen X, Yang W, Mi R, Lu Y, Yang B, Ma M, Shen H. SIRPA enhances osteosarcoma metastasis by stabilizing SP1 and promoting SLC7A3-mediated arginine uptake. *Cancer Lett*. 2023;576:216412.
92. Wang T, Zhang J, Wang J, Pei YH, Qiu XJ, Wang YL. Paclitaxel Drug-eluting Tracheal Stent could reduce Granulation tissue formation in a Canine Model. *Chin Med J (Engl)*. 2016;129:2708–13.
93. Duvvuri M, Motz K, Murphy M, Feeley M, Ding D, Lee A, Elisseeff JH, Hillel AT. Engineering an immunomodulatory drug-eluting stent to treat laryngotracheal stenosis. *Biomater Sci*. 2019;7:1863–74.
94. Zhu GH, Ng AH, Venkatraman SS, Boey FY, Wee AL, Trasti SL, Yee Lim LH: a novel bioabsorbable drug-eluting tracheal stent. *Laryngoscope*. 2011;121:2234–9.
95. Schmä F, Fegeler W, Terpe HJ, Hermann W, Stoll W, Becker K. Bacteria and granulation tissue associated with Montgomery T-tubes. *Laryngoscope*. 2003;113:1394–400.
96. Nouraei SA, Petrou MA, Randhawa PS, Singh A, Howard DJ, Sandhu GS. Bacterial colonization of airway stents: a promoter of granulation tissue formation following laryngotracheal reconstruction. *Arch Otolaryngol Head Neck Surg*. 2006;132:1086–90.
97. Tyler B, Gullotti D, Mangraviti A, Utsuki T, Brem H. Poly(lactic acid) (PLA) controlled delivery carriers for biomedical applications. *Adv Drug Deliv Rev*. 2016;107:163–75.
98. Palani N, Vijayakumar P, Monisha P, Ayyadurai S, Rajadesingu S. Electrospun nanofibers synthesized from polymers incorporated with bioactive compounds for wound healing. *J Nanobiotechnol*. 2024;22:211.
99. Wang Z, Hu W, Wang W, Xiao Y, Chen Y, Wang X. Antibacterial Electrospun Nanofibrous materials for Wound Healing. *Adv Fiber Mater*. 2023;5:107–29.
100. Zhao J, Cui W. Functional Electrospun fibers for local therapy of Cancer. *Adv Fiber Mater*. 2020;2:229–45.
101. Naveenkumar R, Senthilvelan S, Karthikeyan B. A review on the recent developments in Electrospun nanofibers for Drug Delivery. *Biomedical Mater Devices*. 2024;2:342–64.
102. Yang Y, Du Y, Zhang J, Zhang H, Guo B. Structural and functional design of Electrospun nanofibers for Hemostasis and Wound Healing. *Adv Fiber Mater*. 2022;4:1027–57.

Publisher's note

Springer Nature remains neutral with regard to jurisdictional claims in published maps and institutional affiliations.